Alma Mater Studiorum · Università di Bologna

Scuola di Scienze
Dipartimento di Fisica e Astronomia
Corso di Laurea in Fisica

Semi-analytical models for the velocity of a magmatic dike propagating on a curved pathway

Relatore:
Prof.ssa Eleonora Rivalta

Presentata da:
Alberto Polverari

Anno Accademico 2023/2024

Abstract

In questa tesi, analizzo un meccanismo fisico, detto diking, responsabile per il trasporto del magma attraverso la crosta terrestre e la sua eruzione. Il diking è analogo alla fratturazione idraulica, che coinvolge un fluido che si propaga in un solido elastico-fragile creando una sottile fessura, fratturando il solido davanti a sé, fluendo nell'allungamento della fessura appena creato, e lasciandosi dietro una coda che tende a chiudersi. I percorsi delle fratture idrauliche riempite di magma, o dicchi, possono essere non-verticali quando il campo di stress elastico è non-litostatico e spazialmente eterogeneo. La determinazione della velocità di propagazione lungo questi cammini è importante per stimare il tempo disponibile prima dell'inizio di una eruzione. Valuto una stima delle velocità di risalita dei dicchi su percorsi di ascesa non-verticali, combinando una soluzione analitica per la velocità di un dicco con soluzioni semi-analitiche per il campo di stress imposto da carichi gravitazionali, come il carico dovuto ad un edificio vulcanico appoggiato alla superficie terrestre. Sviluppo uno script MatLab che calcola la velocità di ascesa in funzione della profondità. Applico il mio metodo per stimare la velocità di dicchi in classiche configurazioni di stress. Il mio script può essere utilizzato per stimare il tempo di risalita di un volume di magma e, quindi, il tempo disponibile per la gestione dell'emergenza dopo che i segnali precursori vengono individuati.

Abstract

In this thesis, I analyse a physical mechanism, called diking, responsible for the transport of magma through Earth crust and its eruption. Diking is similar to hydraulic fracturing, which involves a fluid propagating in a brittle-elastic solid building a thin crack, fracturing the solid ahead, flowing into the newly-formed crack elongation, and pinching the crack tail shut behind. The pathways of magma-filled hydraulic fractures, or dikes, may be non-vertical when the elastic stress field is non-lithostatic and spatially heterogeneous. Determining the propagation velocity along these pathways is important to estimate the time that is available before eruption onset. I estimate the ascent velocities of dikes on non-vertical ascent pathways, combining an analytical solution for the velocity of a dike with semi-analytical solutions for the stress field imposed by gravitational loads, such as the load due to a volcanic edifice resting on the Earth's surface. I develop a MatLab script calculating the ascending velocity as a function of depth. I apply my method to estimate the velocity of dikes in archetypal stress configurations. My script can be used to estimate the ascent time of a magma batch and, thus, the time available for emergency management after precursory signals are detected.

Contents

Introduction **2**

1 Background to the study of magmatic dikes **6**
- 1.1 Geophysical observations of propagating dikes . . . 8
- 1.2 Theory of elasticity and fracture mechanics . . . 14
- 1.3 Fluid dynamics and rheology of magmas . . . 21

2 Modelling magma transport by diking **24**
- 2.1 Dike formation and self-sustained propagation . . . 25
- 2.2 Interactions with the stress field generated by topographic loading / unloading . . . 31

3 Testing the model against some real diking events **36**
- 3.1 Numerical simulation for a propagating dike below Mt. Etna . . . 38
- 3.2 Numerical simulation for a propagating dike at Campi Flegrei caldera . . . 45

4 Conclusions **52**
- 4.1 Future prospects and implementation . . . 53

A Analytical determination of a critical volume of injection **54**

B MatLab script to simulate dike propagation **56**

Introduction

Volcanoes erupting at the Earth's surface are evidence of the ability of magmas to migrate through the crust from regions of production or storage to the Earth's surface (Tait and Taisne, 2013). The Earth's lithosphere is brittle, meaning that it fractures when stress overcomes a threshold value depending on the type of rock, temperature and pressure conditions. Since permeable or open pathways in the lithosphere are rare and faults tend to heal and become impermeable soon after slippage, usually fluids cannot use pre-existing pathways to ascend. Fluids within the lithosphere may, thus, open their own pathway by fracturing the rock if they are pressurised. This originates hydraulic fractures, which are fluid-filled opening cracks propagating due to the pressure at their tips overcoming the fracture toughness of rock. Dikes (or 'dykes') are magma-filled hydraulic fractures.

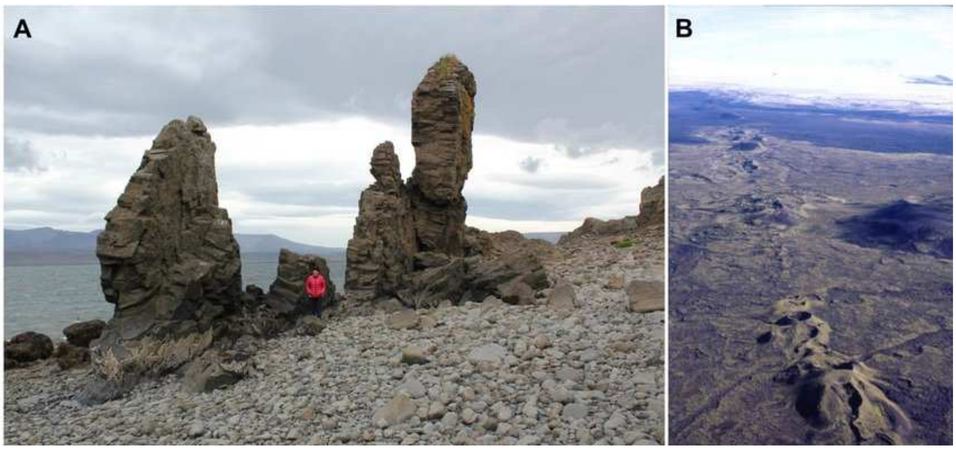

Figure 1: A) A frozen dike on the coast in Southwest Iceland, with a thickness of 3 m (person for scale). B) Part of the volcanic fissure formed during the 1783 Laki eruption in southern Iceland. The feeder dike must have been at least 27 km long. Taken from Gudmundsson et al. (2018).

From field observations at active or extinct volcanoes, we know that melt transport by magma-filled fractures in Earth's crust is an essential physical mechanism contributing to volcanic processes. Eruptive vents and fissures in volcanic settings result from dikes intersecting the surface during their propagation. It is clear, therefore, that the dynamics of dikes is fundamental to the occurrence of volcanic eruptions.

Dikes have also a wider relevance to the dynamics of our planet and to the industry. In fact, they also constitute the main mechanism of plate accretion at divergent boundaries (mid-ocean ridges or continental rifts) (Lister and Kerr, 1991; Wright et al., 2012; Rivalta et al., 2015). Moreover, diamonds are transported to the surface within rapidly-ascending dikes filled with low-viscosity magmas called kimberlites. Furthermore, a mechanism similar to diking is hydraulic fracturing, i.e. the injection of highly-pressurised fluids (e.g. water, CO_2, brine or other fluids) inside rock to enhance rock permeability for geothermal purposes, or to store CO_2 into underground reservoirs, or to retrieve mineral deposits of gas and oil (Rivalta et al., 2015). Hydraulic fracturing is relevant for all fluids injected into brittle-elastic solids, and has considerable relevance to many fields of applied science and engineering.

Dikes are fractures in brittle-elastic rock filled with magma. Therefore, a variety of processes are simultaneously acting and ideally need to be accounted for:

- fluid dynamics of a compressible fluid flowing between moving walls;
- fracture and elasticity of host rock, plasticity at the fracture tips;
- heat transfer which causes phase changes in magmas (crystallisation and bubble nucleation and growth);
- variable physical and rheological properties of magma, as crystallisation may increase magma viscosity by orders of magnitude, while density may decrease substantially if bubbles are present.

A typical approach in physical modelling consists in reducing complexity by examining each aspect on its own first, and subsequently coupling some together to reach a more comprehensive description. By following this procedure, the rich phenomenology of diking can be successfully explained and, at best, the models even show some predictive power.

The first groundbreaking studies about the orientation of dikes in the field were carried out by Anderson (1905), who observed that dikes mostly align perpendicular to the principal stress axis of least compression, and explained this in terms of minimisation of work against the elastic forces in the rock. The first analytical models for the ascent of buoyancy-driven fluid-filled fractures were conducted by Weertman (1971) to model water-filled crevasses in glaciers. Weertman (1980) later applied the same model to dikes.

The study of dike propagation has paramount importance in the realisation of physics-based models of volcanic hazard assessment, as stressed by Rivalta et al. (2019); Mantiloni et al. (2021, 2023). In order to forecast location and time of impending future eruptions, we must rely not solely on past eruptive episodes (this approach is employed in statistics-based models, which may be however heavily limited in volcanic systems where data is scarce), but on determining dike pathways in the crust according to their controlling parameters. This is primarily done, first, by examining and interpreting sequences of ground deformation and seismic swarms prior to possible volcanic activity (Tait and Taisne, 2013), and second, by developing comprehensive models of diking. By calculating the dike pathway, we retrieve the expected location of future eruptive vents (Rivalta et al., 2019). If we can determine their ascent speeds, then we can also forecast whether the magma batch may get arrested on its way, or, if the magma-filled fracture is expected to breach the surface, how much time is available before this occurs. That may be very useful, as lack of information on what to expect increases risks during emergencies. Volcanic areas are sometimes densely populated (cfr. Campi Flegrei in Section 3.2), and the application of physics-based dike propagation models along with statistical ones already in use may contribute to grant longer advance warnings of the likelihood of an eruption, with huge social and economic advantages.

Currently, the Campi Flegrei caldera (CF), which is located 12 km West of the Italian city of Naples and hosts a population of 500k, is in a state of unrest. Ground deformation and seismicity rates have been elevated for a decade and in the last years have shown acceleration. Although this is debated, most scientists think that the magma reservoir, located at a depth between 8 and 4 km, has been replenished as recently as 2012, although it cannot be excluded that this has happened very recently as well. CF has hosted at least three, and maybe up to about ten, caldera forming eruptions, the most recent of which were the Campanian Ignimbrite (39ka), which had a volume of ~ 300 km^3, and the Neapolitan Yellow Tuff (15ka), which had a volume of ~ 40 km^3 (Smith et al., 2011). The last magmatic eruption at the caldera was the 1538 Monte Nuovo eruption (Guidoboni and Ciuccarelli, 2011). Even a small eruption such as Monte Nuovo, which had a volume of 0.025 km^3 (Di Vito et al., 1987), would be disastrous today.

A dike may be in general driven by three factors: magma buoyancy, external stress gradients, and the pressurisation of a feeding source. Dike pathways and ascent velocities strongly depend on the stress field at depth: as mentioned above, stress steers magma trajectories, that are not simply vertical along the crust, while the dip of the trajectory at every point controls the intensity of the buoyancy pressure along the pathway. The stress field anywhere in the Earth's lithosphere is determined by many contributions, the largest of which are the regional (far-field) stresses (in turn determined by plate tectonics), and more local stresses imparted by the load of gravitational loading and unloading generated by topography changes. Other contributions are generated by faulting, intrusions, pressurisation of magma chambers. By combining a model of the stress field at the volcano with a model for the magma trajectories, we can potentially determine the future magma pathways and vent distribution.

In this thesis, I aim to develop a simple model for the ascent velocities of dike intrusions along curved and tilted pathways, and to apply this model to calculate the expected velocity of magma pathways at CF.

In ***Chapter 1***, I will discuss the fundamental results of the theories of elasticity, linear elastic fracture mechanics, fluid dynamics and rheology (i.e. flowing properties) of magma, which need to be combined to provide a complete model of fluid-filled fractures in the brittle crust (i.e. magmatic dikes). Available techniques to gather information on dike propagation (mainly seismic data, deformation data at the Earth's surface and analog methods are considered) will also be listed, together with main observations, at the beginning of the Chapter. In ***Chapter 2***, diking as a physical mechanism of magma transport will be discussed. I will derive an estimate for the ascent speed of dikes in the crust, based on the theories presented in the previous Chapter and some assumptions which are commonly used in all the models formulated in the literature. In addition, the steering effect of surface topography, through gradients in the stress fields that dikes orient to, will be discussed – both pathways and ascent speed are influenced by this interaction. Some real-world diking events will be briefly examined in ***Chapter 3***. I will discuss my results in the context of these events, with particular attention to velocities involved and time intervals before eruptions during which the dikes propagated in the region. With the social importance of these models firm in mind, I will also discuss my models in the context of the current crisis at the Campi Flegrei Caldera. Finally, in ***Chapter 4*** conclusions will be drawn and I will present some aspects which could improve the understanding of the phenomenon of dike propagation, but not treated in this discussion.

Chapter 1

Background to the study of magmatic dikes

Modelling magma transport by diking involves accounting for complex interactions between the brittle-elastic response of cold host rock and the viscous flow of the enclosed fluid. In addition, non-linear rock behaviours such as fracture and plasticity play an important role in the dynamics of propagating magma batches (Rivalta et al., 2015).

As extensively discussed in Rivalta et al. (2015), this challenging coupling of multiple processes has historically led to the development of two approaches, or 'schools', to magma propagation modelling, which simplify the problem in two different ways. In the *toughness-dominated* regime, it is assumed that an inviscid fluid fills the propagating dike (or, simply, the crack). The removal of viscosity effects precludes all information on the timescale of magma transport, but it dramatically simplifies the propagation problem, so that this approach can be used to calculate the dike pathways in a heterogeneous stress field, which is an important requirement at volcanoes. A simple analytical solution in the toughness-dominated regime is the so-called Weertman crack (Weertman, 1971), presented in more detail below (cfr. Section 2.1). In contrast, the *viscosity-dominated* approach neglects energy dissipation by fracturing, so that the fluid dynamics becomes dominant. These latter models output the dike velocity, but the much bigger mathematical complexities involved in solving the flow problem mean that only planar dikes can be considered in this approach. Thus, it is not possible to take into consideration realistic stress fields of volcanoes, which are heterogeneous and would most often induce bending on the dike plane. Moreover, since the tilt of the dike pathway strongly influences the buoyancy force along the trajectory, the velocities calculated on planar pathways are not representative of realistic dike velocities.

Both strategies have clear limitations and are now considered two end-member dike models. Both approaches provide 2-D semi-analytical descriptions and coupled toughness-viscous models have been achieved through numerical modelling. The individual approaches have been generalised to 3-D also through numerical modelling, but coupled 3-D models have not yet been achieved. At the current state of the art, one-way coupling can be used to combine the two approaches: (1) retrieve the dike pathway with a pathway-only model, (2) retrieve dike velocity with a velocity-only model, using the pathway as input. This method was successfully carried out by Pinel et al. (2017).

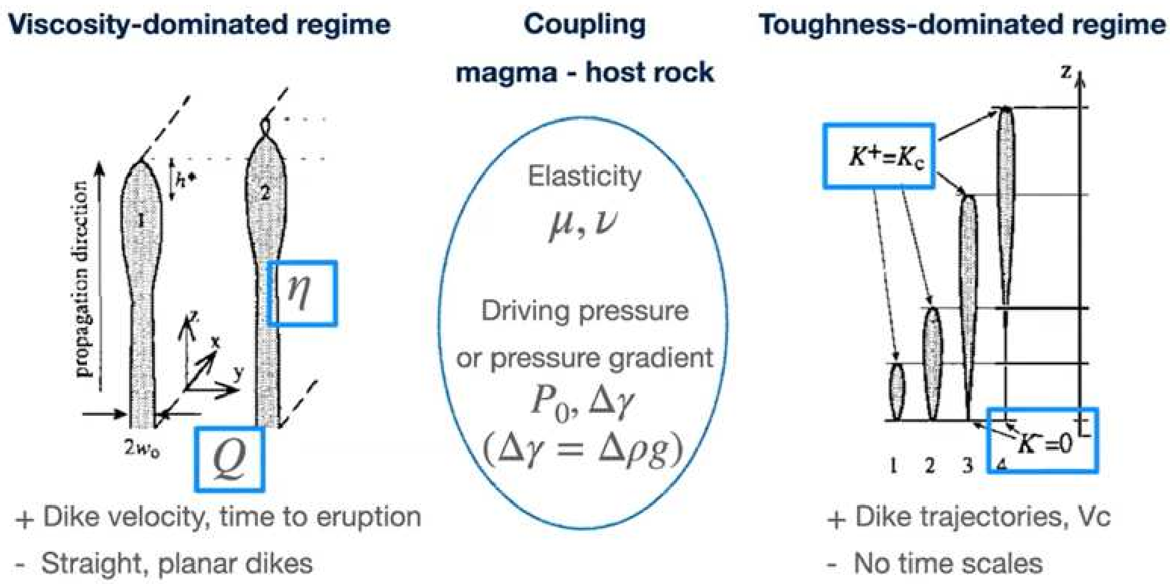

Figure 1.1: Schematic view of the strengths and weaknesses of the two approaches, with the shape they expected for propagating dikes. Taken from Rivalta (2021).

The two approaches result in different dike geometries (Fig. 1.1) and dike propagation dynamics. In the viscosity-dominated regime, a constant-width channel of magma is left behind during propagation, whose thickness is proportional to the fluid viscosity. In order to sustain propagation, coupling with a magma chamber is needed as a source that continuously provides fluid. Thus, constant propagation velocity is obtained only by imposing a constant influx of magma. In contrast, toughness-dominated dikes containing a constant mass can reach 'self-sustained' or 'self-driven' propagation, provided their volume is larger than a minimum volume for propagation, V_c, as better explained in Section 2.1.

Combining these approaches into a comprehensive, although simple, model will be the subject of my thesis, developed in Chapter 2. In this Chapter, I present some preliminary notions. In Section 1.1, I introduce the geophysical observables connected with magma propagation by diking. Observations are well-explained by combining the results of the theories of linear elasticity and linear elastic fracture mechanics (LEFM, for short), which I will present in Section 1.2, with the fluid dynamics and rheological behaviour of magmas discussed in Section 1.3. I evaluate simple canonical states of stress for volcanic regions in Section 1.2, which are main controls on dike pathways and velocities.

1.1 Geophysical observations of propagating dikes

Dikes and sills (their horizontal counterpart) are responsible for transporting magma from great depth (up to 200 km below the surface!) and over vast lateral distances (Rivalta et al., 2024). Propagation of magma by diking causes deformation (strains) and stresses in the host rock (Watanabe et al., 2002; Tait and Taisne, 2013). Stresses are forces acting within a continuous body. These are exerted on the material through its surfaces: normal stresses act perpendicular to a surface, while shear stresses act tangentially along the surface. Thus, stresses are forces per unit area, measured in Pa.

Geological observations of frozen dikes in the field and geophysical signals (in particular, surface deformation, gravity changes and seismicity) acquired during propagation events inform numerical models of propagation.

Field observations In the field, magmatic intrusions are generally found as interconnected systems of solidified dikes and sills, exposed by erosion. We see that sills may be fed by thinner dikes, as shown in Fig. 1.2, and orientations from vertical all the way to horizontal are possible for arrested dikes.

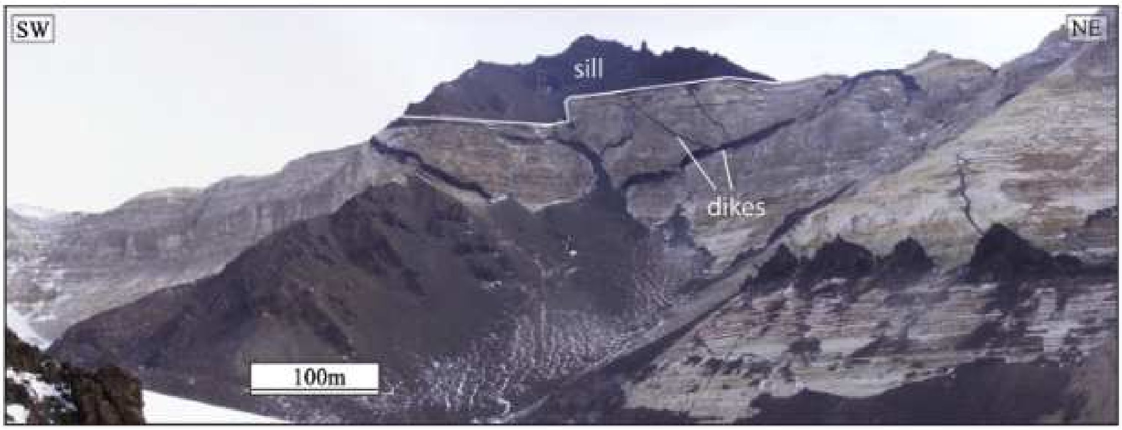

Figure 1.2: Dolerite Ferrar sills and their feeder dikes (Antarctica), from the New Encyclopedia of Volcanoes (Rivalta et al., 2024).

Propagation, however, does not occur at random angles but it is closely connected to the physical properties and stress state of their surrounding environment. Before erupting at the surface, magma may travel significant distances (as much as tens of kilometres) underground, often forcing open new pathways rather than following pre-existing conduits. At some volcanoes showing continuous activity, such as Stromboli volcano in Italy, magmas mostly erupt using a pre-existing conduit, but these conduits are expected to freeze rapidly if they are not supplied with continuous heat. When activity diminishes, a new conduit is then formed by diking.

A common misconception is that existing pathways constitute the only viable conduits for magma transport. Actually, existing pathways may be entirely bypassed, unless they are favoured considering the stress state in the region (Rivalta, 2021). However, stresses are continuously variable in volcanic settings (see the components of stress listed in Section 1.1, all of them varying with different timescales), so that eruptions do not happen always from the same fissure. Eruptive episodes in turn change the loading state by deposition of products, and dikes move on other new pathways.

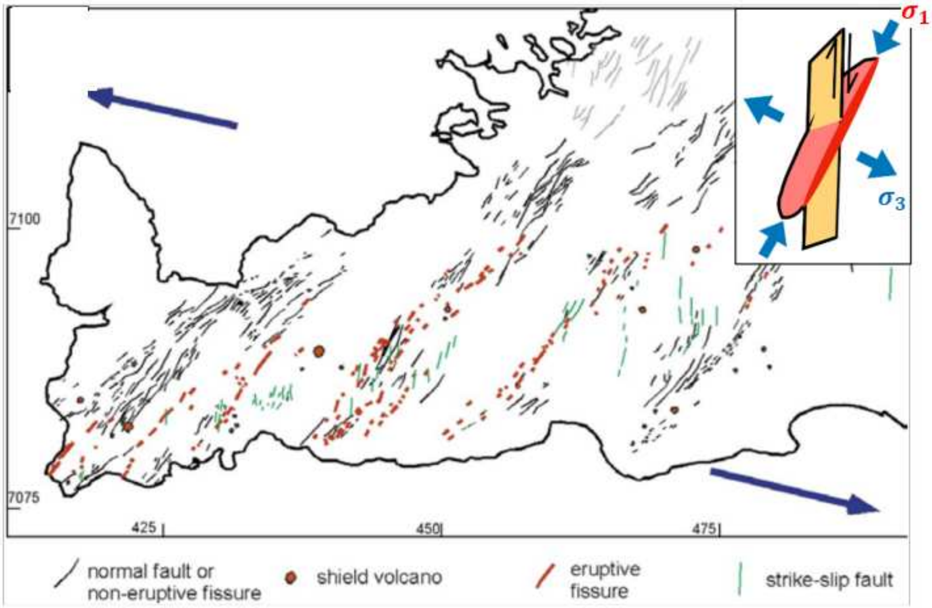

Figure 1.3: Orientation of eruptive fissures (red) and strike-slip faults (green) in the Reykjanes peninsula (inset: expected orientation according to the Anderson theory). Modified from Rivalta et al. (2024).

Moreover, magma channelling through pre-existing faults, although often proposed, is infrequently found in the field (Rivalta et al., 2024). In fact, dikes orientation pattern is considerably different from the one of shear-fractures, i.e., faults in the Earth's lithosphere, which tend to orient in order to encourage sliding between plates without opening walls (Rivalta, 2024). Large work against elastic forces would thus be needed to dilate the two walls of a fault. Fluid-filled fractures, instead, have to accommodate a volume and thus will optimise according to this criterion. This can be seen in the field, where it becomes evident that dikes and faults orient themselves according to different patterns, once the stress state of the region is known. The best examples are found in areas of gentle topography such as the Reykjanes peninsula in Iceland (Rivalta et al., 2024). There, NE-SW-oriented eruptive fissures cross-cut N-S oriented strike-slip faults, as shown in Fig. 1.3.

As explained by Dahm (2000a), an opening fracture will minimise the work done against elastic forces if it opens perpendicularly to the direction of the minimum compressive stress σ_3 (that is, aligned to the maximum compressive stress, σ_1).

The condition of minimum work done against elastic forces actually paves the way for numerical integration of dike pathways - in every point, the direction of the maximum and minimum compressive stresses are found by numerical procedures and thus the direction of new increment of the fracture length is identified. These simulations only pertain to toughness-dominated regimes of dike behaviour; hence they give little to none information about dike velocities along the path.

In the field, we observe dikes sometimes get arrested at layer discontinuities, or suddenly changing their propagation direction. Sometimes, they keep on propagating basically unaffected by any structural complexity in the host rock.

The shape of magmatic intrusions is inferred from the two-dimensional cross sections of frozen dikes in the field, by mapping the contact between solidified magma and its host rock. The third dimension is then usually obtained by typical values of aspect ratio (thickness / breadth), once the thickness of the fracture's aperture is measured. As stated in Rivalta et al. (2024), magma compositions that are higher in silica, and therefore higher viscosity, have a higher aspect ratio.

Seismic observations When shear stresses build up in the crust, surfaces previously held together by friction may suddenly start to slip in opposite direction. This process is known as 'failure', or 'earthquake', and results in seismicity.

As far as propagating dikes are concerned, small earthquakes appear in 'clouds' or 'swarms' and are due to the high stress concentration at the fracture's tip (see Section 1.2), causing host rock to fail with the advancing head of the dike. Localisation of hypocentres in these seismic swarms provides insight into the geometry of the pathway of ascending magmas. As shown in Fig. 1.4, propagation is rarely only vertical and curved pathways are common, according to the stress field at depth.

Moreover, since the clouds of earthquakes induced by propagating dikes are migrating, the dikes' ascent velocities may be constrained from the time evolution of the swarms (Rivalta et al., 2024). Geophysically-inferred dike velocities range from 1 km/day to a few km/hour. These are in agreement with petrological evidence: it is required that dikes propagate rather fast in order not to solidify at depth, and transport minerals, such as diamonds, up to the surface, without damaging them.

Dikes might decelerate or accelerate during their ascent, especially when close to the

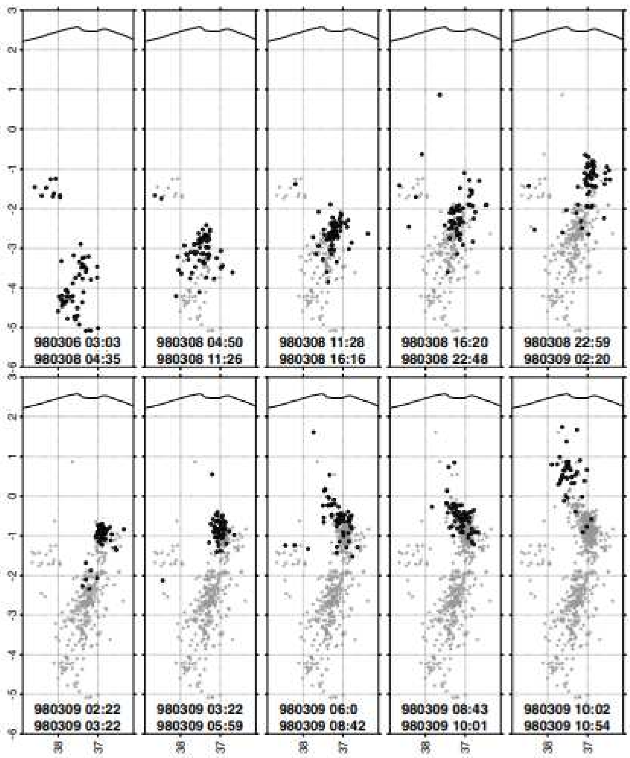

Figure 1.4: Spatio-temporal evolution of hypocentres along a cross-section of Piton de la Fournaise volcano, preceding the 1998 eruption. Each plot shows by black marks the events which occurred between the dates given at the bottom of the plot. In addition, the events which occurred prior to those 100 earthquakes are plotted by grey marks. The lower-right plot shows all the located events of the pre-eruption swarm. Taken from Battaglia et al. (2005).

surface where topography is highly heterogeneous. Acceleration is often the preamble of an eruption, while slowing dikes get typically stalled and freeze under the surface.

Geodetic observations Typical strain values for geophysical materials in laboratory experiments are $\epsilon \sim 10^{-8} - 10^{-9}$ (that is, a variation of $\sim \mu$m over a length of ~ 1 km). Tectonic deformation rates are of the order of $\sim$ cm/year. Propagating dikes, in contrast, induce much higher strain rates around their propagating tip. The ground above dike intrusions can deform as fast as cm/hour as dikes approach the Earth's surface. Dike intrusions are quite easily recognised based on geodetic observations, since they create distinctive patterns of ground deformation (Rivalta et al., 2024). Magma inside dikes forces the opening of the dike walls, causing an uplift of rock volumes adjacent to the dike. Directly above the dike, in contrast, we observe subsidence due to the upper tip-line of the crack being pulled down. At the surface, these intense strains concentrated in a very small region may result in faulting, especially when dikes reach shallow depths.

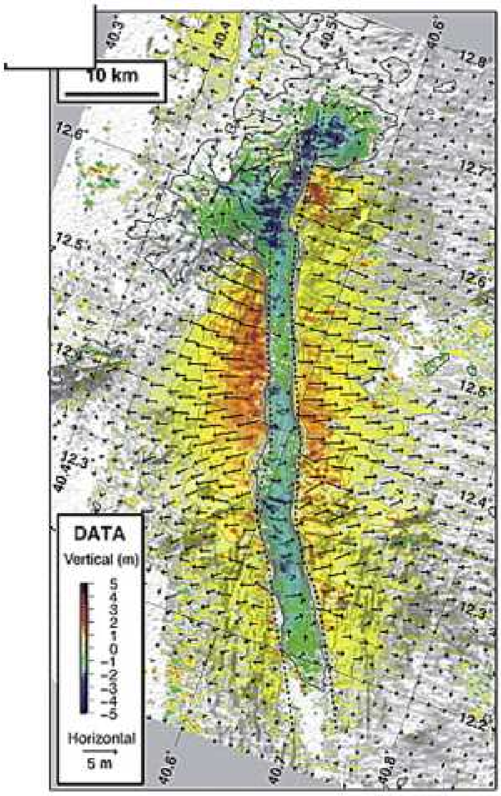

Figure 1.5: Surface displacements at Manda Hararo volcanoes, Afar (Ethiopia) during the 2005 dike event. Vectors show horizontal displacements, colours show vertical displacements. Taken from Rivalta et al. (2024)

Geodetic monitoring techniques, such as GPS/GNSS or InSAR, are fundamental tools used to detect and record ground swelling around volcanoes. These data can then be matched to mathematical models describing the expected deformation for different volume change geometries at depth. We then retrieve information (volume and spatial distribution of magmatic intrusions) about deformation sources underneath the ground by inversion. The volumes of geophysically-observed dikes from the last decades range from about 10^5 m^3 up to a few km^3 Rivalta et al. (2024).

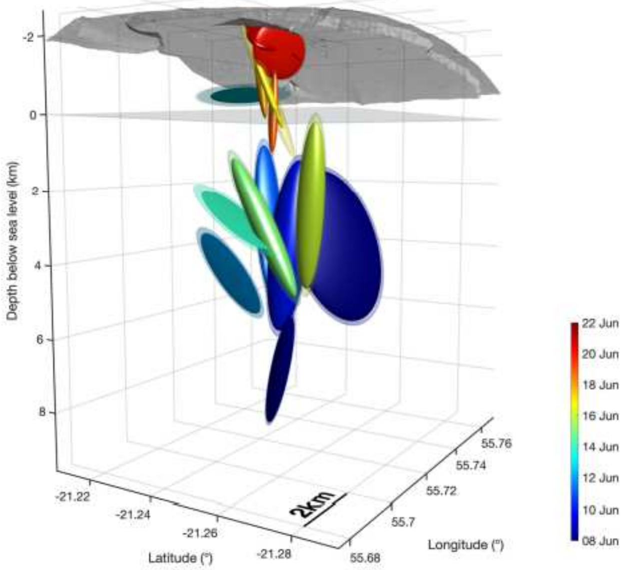

Figure 1.6: Different time-dependent inversion models from Beauducel et al. (2020), employed during the June 2014 pre-eruptive unrest at Piton de la Forunaise volcano. Colours stand for the most recent date of each time window. Size of each source is proportional to its associated volume variation. Transparent plain at depth = 0 km simulates the sea level.

Geophysical analog models It is impossible to directly observe subsurface magma ascent, and it is impossible to reproduce this with realistic experimental conditions in the laboratory. Therefore, analog models are ordinarily employed. The rationale behind these models is that although physical quantities are several order of magnitude less than in real-world situations, there exist some adimensional numbers controlling the dynamics of the process (e.g. the Reynolds number) that are kept constant for the laboratory and the real setting.

Magma dikes can be visualised on a laboratory-scale through air or water injections in gelatin in a transparent container, as carried out by, for example, Dahm (2000a) or Watanabe et al. (2002). Once air gets injected through a small hole at the bottom of the container, a crack forms, since air density is much smaller than gelatin's. The crack has an 'inverse teardrop' shape (see Fig. 1.7 and Fig.1.8). Only when enough air volume is introduced, the fracture starts propagating slowly (Rivalta et al., 2024).

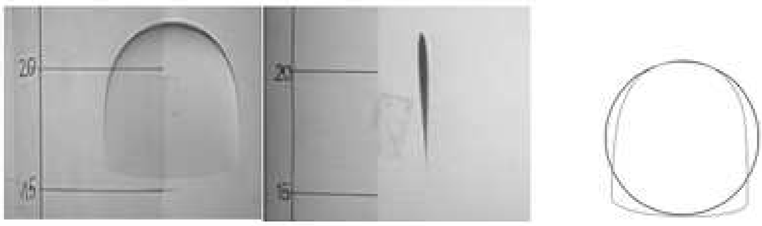

Figure 1.7: Left: Shape of an ascending air-filled crack in gelatine. Right: Air-filled cracks tipline versus a penny-shaped tipline. Taken from Davis et al. (2020).

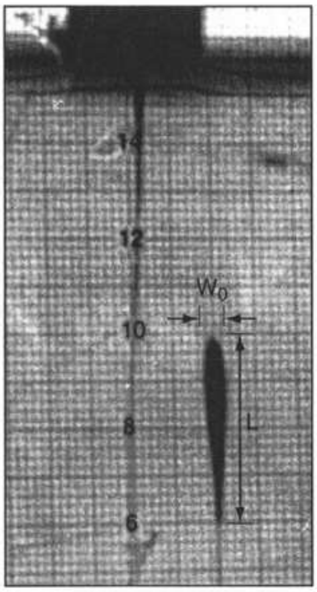

Figure 1.8: Photograph of an experimental air-filled dike during propagation. Taken from Muller et al. (2001).

1.2 Theory of elasticity and fracture mechanics

Materials are called elastic if they deform upon the application of a force and return to their original shape when the force is removed (Turcotte and Schubert, 2014, p.185). The prototype of elastic behaviour is the spring, described by Hooke's Law:

$$\mathbf{F} = k\Delta\mathbf{u} \tag{1.1}$$

where the force applied to the system $\mathbf{F}$ and displacement $\Delta\mathbf{u}$ are linearly proportional by a material constant.

In the mechanical description of continuous bodies, Hooke's law is generalised by the introduction of the concepts of stress and strain, already defined in Section 1.1. These physical quantities enjoy a mathematical description as the tensors σ_{ij} and ε_{ij}, respectively. Tensors can be decomposed in an isotropic component and a deviatoric component. For a linear elastic material, the following relations hold between the isotropic and the deviatoric components of stress an strain, respectively:

$$\frac{1}{3}\sigma_{kk} = K\varepsilon_{kk} \quad (K > 0) \tag{1.2}$$

$$\sigma'_{ij} = 2\mu\varepsilon'_{ij} \quad (\mu > 0) \tag{1.3}$$

The resulting generalised Hooke's law relating stress and strain reads as:

$$\sigma_{ij} = 2\mu\varepsilon_{ij} + \left(K - \frac{2}{3}\mu\right)\varepsilon_{kk}\delta_{ij} \tag{1.4}$$

This is the constitutive equation for linear elastic solids (see rheology in Section 1.3). By coupling this equation with the momentum conservation for continuous bodies, we obtain the Cauchy-Navier equations for isotropic, homogeneous elastic media. By solving the system of equations, the displacement field $\mathbf{u}$ is known for the material, once the external forces are given.

Rocks, as any other solid material, present an elastic behaviour whenever:

i. applied stresses last relatively short times;

ii. stresses do not approach the resistance limit of the rock;

Elasticity provides a valid description for crustal rocks at relatively low temperatures and confining pressures in the lithosphere.

Stress state in the lithosphere At great depth within the Earth's crust, it is reasonable to assume that the state of stress, at least to a first approximation, is lithostatic:

$$\sigma_{xx} = \sigma_{yy} = \sigma_{zz} = \frac{1}{3}\sigma_{kk} \equiv p_{lit} \tag{1.5}$$

This corresponds to a isotropic stress tensor $\sigma_{ij} = p_{lit}\delta_{ij}$, and by solving the equations of equilibrium one obtains for lithostatic pressure:

$$p_{lit}(z) = -\rho_r g z \tag{1.6}$$

where z is the vertical coordinate, here taken positive upward, and ρ_r is the density of the host rock.

Note that here and in the following discussion, we adopt the convention of considering compressive stresses as positive.

With increasing depth, temperature increases and anelastic processes of deformation become more and more effective, leading to a relaxation of deviatoric stress (i.e., off-diagonal components of σ_{ij} becoming negligible).

This assumption, however, does not work well for volcanic settings, where many processes may lead to the build-up of non-lithostatic stresses.

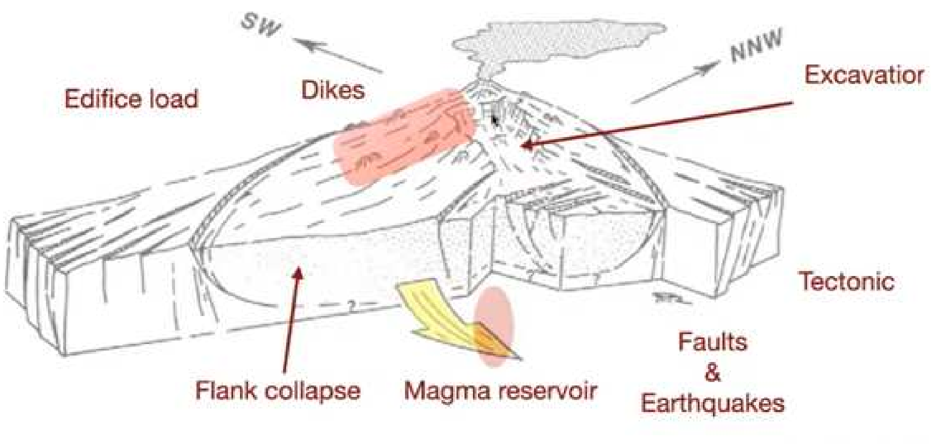

Figure 1.9: Schematic representation of the different sources of stress that may be present at volcanoes. Adapted from Rivalta (2021)

Contributions to the stress field in volcanic settings include, roughly from larger to smaller in intensity and spatial 'reach' (Rivalta et al., 2019):

- tectonic stress;
- loading due to volcanic edifice loading;
- edifice unloading e.g due to caldera collapse, landslides and flank collapses;
- intruded dikes;
- pressurisation of magma reservoir;
- major faults and earthquakes.

The stress state at volcanoes is, thus, complex and would require accurate, dedicated modelling. Here, I will take a simple approach to the problem, by only considering gravitational loading and unloading and by considering simple edifice or caldera geometries.

The stresses induced by topographic loading A fundamental class of problems in elastostatics is computing the stress and displacement in every point of an infinite elastic half-space when a force is applied normally in a point P of the its surface. This is usually referred to as Boussinesq problem (1878). Jaeger et al. (1969) delivers the 3-D solution for the Boussinesq problem for a point load:

$$\sigma_{xx} = \frac{N}{2\pi}\left(\frac{3x^2z}{r^5} + \frac{(1-2\nu)(y^2+z^2)}{r^3(z+r)} - \frac{(1-2\nu)z}{r^3} - \frac{(1-2\nu)x^2}{r^2(z+r)^2}\right)$$

$$\sigma_{yy} = \frac{N}{2\pi}\left(\frac{3y^2z}{r^5} + \frac{(1-2\nu)(x^2+z^2)}{r^3(z+r)} - \frac{(1-2\nu)z}{r^3} - \frac{(1-2\nu)y^2}{r^2(z+r)^2}\right)$$

$$\sigma_{zz} = \frac{N}{2\pi}\left(\frac{3z^3}{r^5}\right)$$

$$\sigma_{xy} = \frac{N}{2\pi}\left(\frac{3xyz}{r^5} - \frac{(1-2\nu)xy(z+2r)}{r^3(z+r)^2}\right)$$

$$\sigma_{yz} = \frac{N}{2\pi}\left(\frac{3yz^2}{r^5}\right)$$

$$\sigma_{xz} = \frac{N}{2\pi}\left(\frac{3xz^2}{r^5}\right)$$

where r is the distance from the origin to the point (x, y, z).

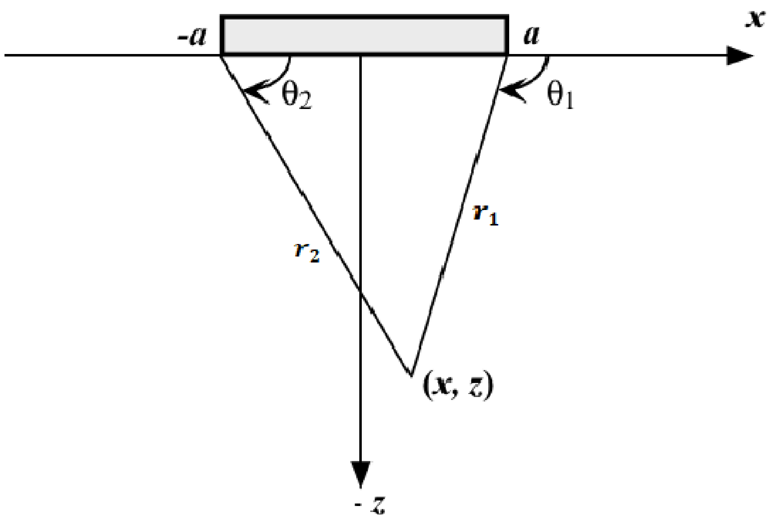

Figure 1.10: Configuration with a strip load above the free surface. Modified from Watanabe et al. (2002)

If the total force is distributed over an infinitesimal strip of width dx, then $N = Pdx$ and the solution for a 2-D strip loading is obtained by integration for $-a \leq x \leq +a$. We also impose a plain strain configuration, that is, whenever one dimension in a system is very large compared to the others, one may assume that strains in that direction are negligible. In plain-strain elasticity, thus, we consider only a cross section (the $x - z$ plane of interest) with the fracture having 'infinite' extension along the third dimension (y axis). Earlier studies account for $10^{-2} - 10^{-4}$ as typical values of aspect ratios of dikes (Rubin, 1995). Hence, they are often approximated as planar sheets, as I will discuss in Section 2.1. This assumption remains accurate exclusively along a central axis if the fracture is sufficiently broad in the y direction (Davis et al., 2023).

From Eq. 1.4, if we impose $\varepsilon_{yy} = 0$, one can easily obtain the condition:

$$\sigma_{yy} = \nu \left(\sigma_{xx} + \sigma_{zz}\right) \tag{1.7}$$

Jaeger et al. (1969) provides the following expressions for the stress tensor components:

$$\sigma_{xx} = \frac{P}{\pi}\left(\left(\theta_1 - \theta_2\right) - \sin\left(\theta_1 - \theta_2\right)\cos\left(\theta_1 + \theta_2\right)\right)$$

$$\sigma_{zz} = \frac{P}{\pi}\left(\left(\theta_1 - \theta_2\right) + \sin\left(\theta_1 - \theta_2\right)\cos\left(\theta_1 + \theta_2\right)\right)$$

$$\sigma_{xz} = \frac{P}{\pi}\left(\sin\left(\theta_1 - \theta_2\right)\sin\left(\theta_1 + \theta_2\right)\right)$$

where the angles are defined in Fig. 1.10. A solution is also possible in terms of the angles θ_1, θ_2 and the radii r_1, r_2. By substituting P with $-P$, one obtains a stress state to model the unloading due to surface mass removal.

Similar equations are also valid for a triangle-shaped load and can be found in Dahm (2000a).

Fracture and plasticity To a first approximation, elasticity may be adopted to describe the behaviour of lithospheric rocks in which dikes propagate. However, in the region in front of the dike tip, where strains are very intense and temperatures may be a significant fraction of the rock solidus, we encounter significant deviations from an ideal elastic behaviour.

At low temperatures and confining pressures, rocks are brittle-elastic solids, and large deviatoric stresses cause fracture (Turcotte and Schubert, 2014, p.185). Whether lithospheric rock will respond elastically or in a brittle fashion to an external perturbation dramatically depends on the duration of the imposed stress. In order to induce fracturing in the material, the timescale of transport of the perturbation needs to be much shorter than the timescale of relaxation of the medium (Rivalta, 2024).

Fracturing is a non-linear, irreversible process that generates a displacement discontinuity $\Delta\mathbf{u}$, or slip, along specific planes in the material. Another non-linear behaviour is plastic deformation. Like fracturing, it is valid for rock at high confining pressures, but in different thermodynamic conditions. If deformation is plastic, the material yields in a widespread, continuous manner, much like a fluid. The difference between brittle and plastic response under some imposed stress is shown in Fig. 1.11.

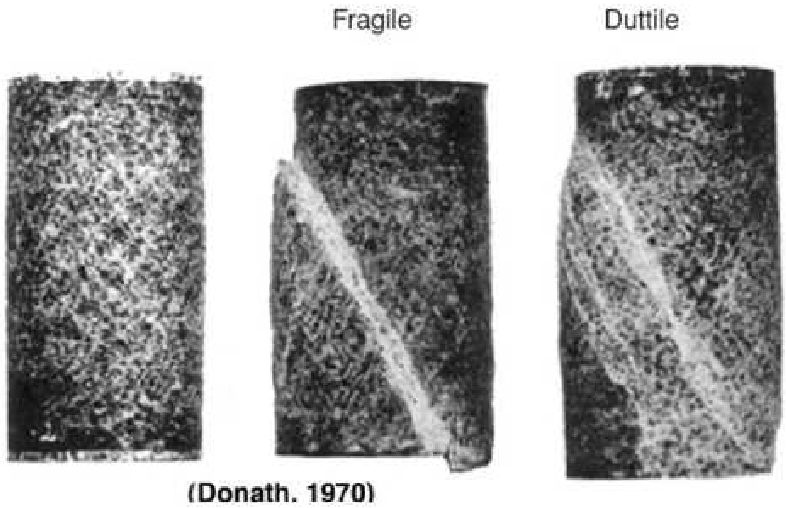

Figure 1.11: Differences in fragile and ductile behaviour for a rock sample. Taken from Rivalta (2024).

Slip may be parallel to the fracture plane, giving rise to shear fractures, or faults (Mode II fracturing, or Sliding Mode, and Mode III fracturing, or Tearing Mode), as explained in Jaeger et al. (1969, p.88). Dikes are predominantly tensile cracks, that is, the two walls of the fracture move apart in a direction perpendicular to the plane of the crack (Mode I fracturing, or Opening Mode), with magma occupying the intervening space. Different modes of fracturing are presented in Fig. 1.12.

Lithostatic stress at $z = 5$ km depth is of the order of ~ 100 MPa, and is therefore sufficient to pinch close any tensile crack that may generate within the crust. However, if the fracture is filled with a pressurised fluid, the overpressure against crack wall may generate enough stress to overcome the lithostatic pressure of the host rock, and get the fracture to stay open, as discussed in Chapter 2.

Linear Elastic Fracture Mechanics (LEFM) has addressed the problem of determining the stress state near the tip of a tensile crack. In a local polar coordinate system (see Fig. 1.13), with its origin at the crack's tip, the stress field can be expressed as:

$$\sigma_{ij} = \frac{K}{\sqrt{2\pi r}} f_{ij}(\theta) + O(r) \tag{1.8}$$

At the crack tip line, thus, the predicted stress becomes singular ($r \to 0$), and its intensity depends on the stress intensity factor K for mode-I fracturing. This quantity

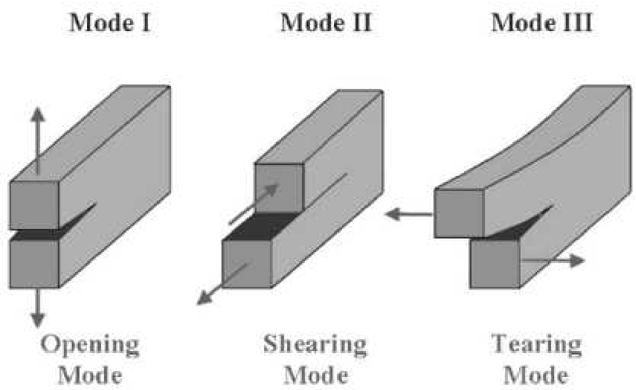

Figure 1.12: Schematic view of different fracture modes. Taken from Rountree et al. (2002).

is defined once the crack geometry and the stress applied are known - thus, it can be found analytically, numerically or even experimentally measured.

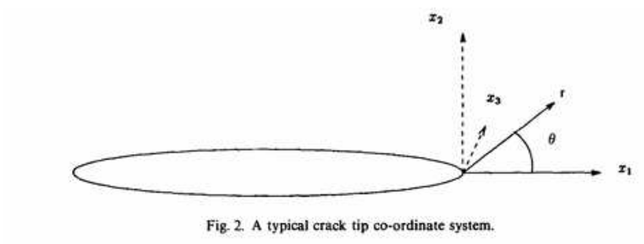

Figure 1.13: Schematic view of coordinate system at the crack tip. Taken from Atkinson and Craster (1995).

As far as the study of dike propagation is concerned, we will be interested in determining a condition under which brittle fracture are allowed to start forming and, conversely, what conditions cause dikes to cease propagating (Parfitt and Wilson, 2008). Fracture occurs when stress at the crack tip overcomes a threshold at which molecular bonds are broken,

$$\sigma > \sigma_{crit} \tag{1.9}$$

From Eq. 1.8, the order of magnitude of stress near the fracture will depend on its K. Thus, the propagation criterion expressed with stress values is substituted by a condition on the stress intensity factor and a critical value for $K > K^* = K_c$. This quantity is actually a rock property and it is called the fracture toughness. This represents a measure of the maximum intensity of stress that the mineral grains at the dike tip can withstand before failing, and is the parameter actually controlling the processes of magma propagation and arrest by diking, as we will see in Chapter 2.

As suggested by Rubin (1995), when dealing with the propagation of tensile cracks, a useful distinction between three regions is made:

- the crack, where the material faces are completely separated;
- the intact host material, where deformation is essentially elastic (or in general is adequately described by some other continuum model). Some (Rubin, 1993) also consider a possible visco-elastic behaviour for host rock, in order to account for different timescales of intrusions.
- an intermediate region surrounding the crack tip, the so-called ‘process zone’, where the strength of the material has been exceeded and inelastic deformation occurs rather than brittle fracturing. This region is effectively described by elasto-plastic fracture mechanics. In the process zone, or damage zone, a lot of microcracks are present. When the dikes become bigger, the process zone widens too, this can be accompanied by earthquakes. These lead to dissipation of energy and their effect on the elastic energy of the system should be included. This, eventually, also increases fracture toughness. This is the reason why we cannot use laboratory values of K_c for dike propagation in the field; instead, we use an ‘efficient’ fracture toughness K_c^{eff} some orders of magnitude larger (scale-dependency).

The divergent stress profile close to the crack tip reaches the yield strength of the material at some distance from the crack tip. Inside the region, the material is plastic (microcracks form), outside is linear elastic. A criterion establishes whether we can expect propagation of the crack tip.

1.3 Fluid dynamics and rheology of magmas

Solids undergo finite deformation upon being stressed. In contrast, when a shear stress is applied to a fluid, this responds by flowing: Newtonian fluids are characterised by a linear relationship between stresses and *rates* of strain $\dot{\varepsilon}_{ij}$.

Elastic solid	Newtonian fluid
$\sigma'_{ij} = 2\mu\varepsilon'_{ij}$	$\sigma'_{ij} = 2\eta\dot{\varepsilon}'_{ij}$

The definitions of strain and strain rate are, respectively:

$$\varepsilon_{ij} = \frac{1}{2}\left(\frac{\partial u_i}{\partial x_j} + \frac{\partial u_j}{\partial x_i}\right) \qquad \dot{\varepsilon}_{ij} = \frac{1}{2}\left(\frac{\partial v_i}{\partial x_j} + \frac{\partial v_j}{\partial x_i}\right)$$

While strain is the result of a gradient in the displacement of elements of the solid from its equilibrium position, strain rates are the result of gradients in the velocities of displacements of fluid elements. As stated by (Turcotte and Schubert, 2014, p.411), a rheological law for the fluid is the equation that relates imposed stresses to velocity gradients in the fluid.

Rheology is the branch of science which studies the 'flow' of materials under some imposed forces (e.g. a given state of stress). Many applications are found in fields of medicine (emo-rheology), food industry, engineering, mathematics and geophysics. The rheological behaviour of materials is described by a so-called constitutive equation - an assertion about mechanical properties of the material in the form of a mathematical functional relation between stress and strain (and their time-derivatives).

Crystal-free and bubble-free magmas behave as viscous fluids, or 'Newtonian' (Rubin, 1995).

Lubrication approximation of fluid dynamics In a fully bounded fluid, lubrication theory is used to determine the pressure distribution on the fluid volume. It can be used whenever one dimension of fluid flow is significantly smaller than the others. Dike length scale L, along the z axis, is always some order of magnitude greater than the fracture's aperture w, along the x axis (see Fig. 1.14).

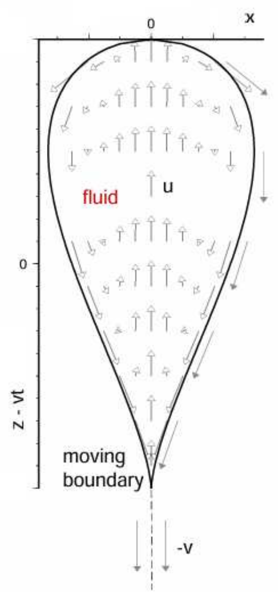

Figure 1.14: Schematic view of the dynamics of fluid-filled fractures in Dahm (2000b). Actual fractures are even thinner in their extension along the x axis.

This determines an approximation to the Navier-Stokes equations governing fluid flow, which are written as:

$$\begin{cases} \frac{\partial p}{\partial x} = 0 \\ \frac{\partial p}{\partial z} - \rho_m g = \eta \frac{\partial^2 u_z}{\partial x^2} \end{cases} \tag{1.10}$$

that is, pressure variations are neglected along the least significant dimension. The vertical component of the velocity $u_z(x)$ is described by Hagen-Poiseuille flow for a fluid filling a plane fracture with a moving boundary:

$$u_z(x) = \frac{1}{2\eta} \left(-\frac{dp_{visc}}{dz} \right) \left(h^2 - x^2 \right) - v \tag{1.11}$$

where the pressure decreases in the increasing z direction, so that the pressure drop dp_{visc}/dz is negative.

Since everything is stationary, the net flow over a horizontal line within the fracture must be zero (Dahm, 2000b). By imposing the condition

$$\int_{-h}^{+h} u_z(x)\, dx = 0 \tag{1.12}$$

one obtains a useful equation relating viscous pressure drop and velocity of the filling fluid:

$$\frac{dp_{visc}}{dz} = -\frac{3\eta}{h^2} v \tag{1.13}$$

Very recently Furst et al. (2023) have combined fluid flow with dike trajectory in 2D. Dahm (2000b) already paved the way for this result. However, a coupling for the 3D problem is still missing.

Chapter 2

Modelling magma transport by diking

Magma transport through the brittle crust occurs by diking, i.e., the propagation of magma-filled fractures (Rubin, 1995). In industrial contexts, the same mechanism is also called hydraulic fracturing.

The evidence that this process is prevalent compared to other proposed mechanisms lies in observing the geometry of ascending magma-filled bodies, as described in Chapter 1. Porous flow, for example, is a very important mechanism for magma ascent but limited to regions of high permeability, which are typically restricted to the deep regions where partial melting occurs, and to regions internal to magma reservoirs, where temperature is high and partial melt is thermally stable. There, porous flow is responsible for the migration of small melt pockets that would have not had sufficient overpressure to fracture the more rigid rock matrix (Rubin, 1995).

Igneous bodies in the field include large granitic diapirs (e.g. the rocks constituting much of the Alps), which have a more rounded aspect ratio than dikes. Diapirism, i.e. the slow ascent of high-viscosity magmas in the viscoelastic deep crust, was historically considered as a common mechanism for the uprise of magma through the crust (Rubin, 1993). However, ascent velocities predicted by a fluid dynamical model of diapirism are too low even in hot crustal layers, and zero closer to Earth surface (Dahm, 2000a). Solidification would prematurely arrest rising diapirs of magma. Currently, diapirs in the field are interpreted as the ballooning of dikes filled with granitic magmas which became arrested and inflated post-arrest through uprise of further magma contained in the intrusion tail (McCarthy et al., 2015).

Diking, therefore, constitutes a viable model of rapid ascent of magmas of all compositions (Cruden and Weinberg, 2018). Propagation velocities from analysis of seismicity induced at the tips of propagating dikes range from about 0.1 to about 1 m/s. These velocities allow dike intrusions to travel long distances in few days (Davis et al., 2023), with little or no significant solidification, as suggested by Dahm (2000a). Since diking events usually enfold in the time span of a few hours to a few days, physics-based models are not only important for a better understanding of the physical mechanisms promoting volcanic eruptions, but they can also support hazard assessment, and could potentially lead to real-time physics-based forecasting of magma ascent towards the surface. In addition, data-driven approaches are commonly employed in forecasting models. Albeit very successful in a wide range of contexts, these may perform poorly in volcanic settings where a great deal of data is lacking.

Diking is predominant in the upper crust, as it requires rocks with a brittle behaviour. In the lower part of the crust, where ambient pressures and temperatures favour a ductile behaviour for rock, diking is inhibited. However, observations of seismicity migrations clustering on flat bodies in the lower crust or even the lithospheric mantle exist (Cesca et al., 2020; Wilding et al., 2023). Brittle fracturing of magmas at high temperature is also possible whenever there is a sufficiently high contrast in viscosity with the enclosed fluid and when strain rates are relatively high due to the rapid propagation (Rubin, 1993; Tuffen et al., 2008). Timescales are thus fundamental to consider when considering the plausibility of a diking model.

2.1 Dike formation and self-sustained propagation

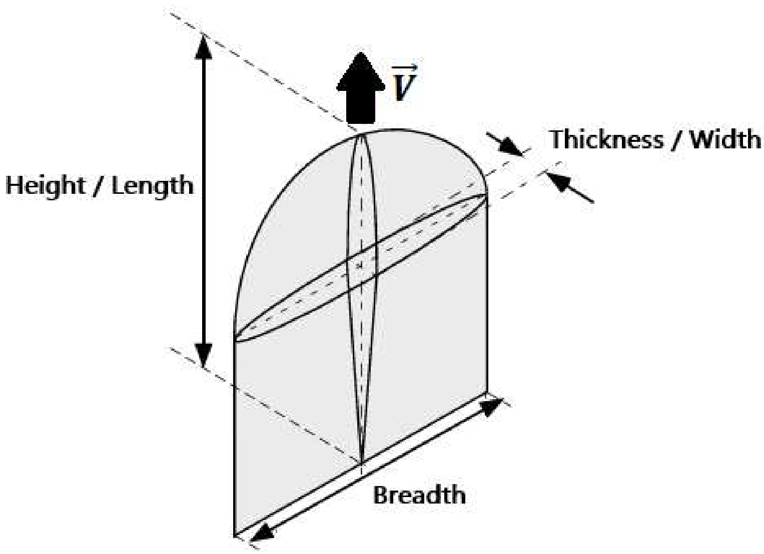

Figure 2.1: Shape of a dike with its characteristic dimensions. The propagation direction is also marked by an arrow. Modified from Watanabe et al. (2002)

Dikes are sheet-like (sometimes referred to as ‘tabular’) magma intrusions. Consistently with empirical observation, three characteristic dimensions are defined (refer to Fig. 2.1):

- length $L = 2a$ (also called height for vertical dikes); it is the longest dimension, with typical values in the range: 100 m $< L <$ 10 km.
- thickness, or width $w = 2h$; typically, one has 10 cm $< w <$ 10 m.
- breadth B, or lateral extent; for vertical propagating dikes, one always has $B < L$ with values in the range 1 km $< B <$ 10 km.

Width is typically, as seen in the field, much smaller than length and breadth (vertical and horizontal extents, respectively), so dikes are often reasonably approximated as 2-D sheets in plain strain condition (see Fig. 2.2) - only a cross section along the breadth dimension is considered so that B becomes irrelevant. 3-D models often use penny-shaped cracks, so that the two horizontal dimensions (L and B) are actually both equal to $2a$ (see Fig. 2.3).

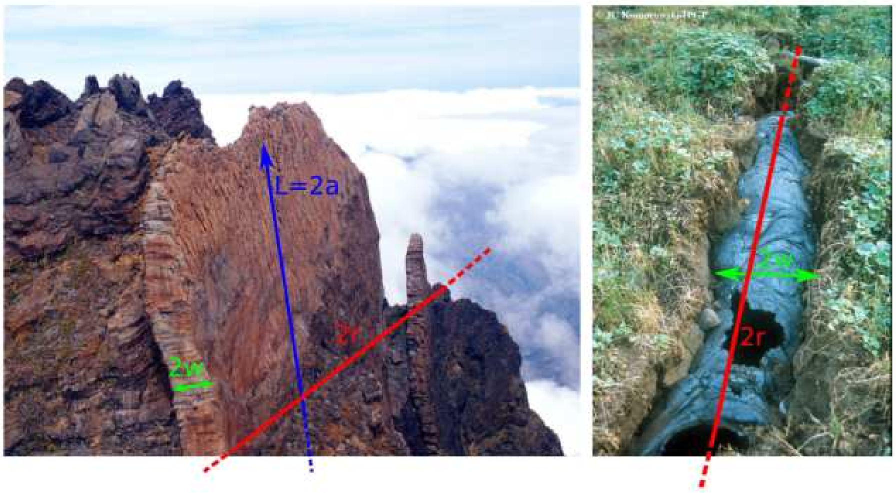

Figure 2.2: Dimensions of dikes from the field. Left: Dike exposed by erosion on Piton des Neiges, Reunion Island. Right: Dike reaching the surface at Nyiragongo. Taken from Smittarello (2019).

As pointed out in Section 1.1, according to fracture mechanics principles, a fracture in a brittle material (in our discussion, cold rock in the upper lithosphere) can extend if the stress overcomes a critical threshold, and this condition is represented by the stress intensity factor at the fracture tip, K, being greater than the rock's fracture toughness K_c.

Dynamic propagation of magma-filled cracks is driven by three main factors, which can act simultaneously or in isolation: (Nakashima, 1993)

1. the buoyancy of magma with respect to the host rock;

2. the external stress field;

3. the pressurisation of a magma chamber feeding the dike.

The last point refers to the fact that if the dike is connected to a magma reservoir, it gains an additional overpressure. However, once the dike has begun its propagation, the chamber de-pressurises and does not contribute significantly anymore at later times. For simplicity, in this thesis I concentrate on the first and second driving factors, and neglect the feeding pressure of a magma chamber. This contribution can be added in future studies.

The force balance between internal magma pressure p_{int} and elastic stresses of host rock directed normally to the dike aperture, σ_n, is referred to as the 'overpressure' of the dike with respect to the surrounding environment:

$$\delta p_0 = p_{int} + \sigma_n \tag{2.1}$$

It represents an important boundary condition to the problem of coupling elasticity and fluid dynamics.

Fluid-filled fractures are expected to change their shape as a result of the equilibrium between internal and external pressure. This way, they may reach a condition that leads them to propagate (Dahm, 2000a). For uniform loading stresses, the elastostatic solution for the dike thickness profile is elliptical and the thickness w at the centre is: (Rubin, 1995)

$$w(0) = 2h(0) = \frac{1-\nu}{\mu}\delta p_0 2a \tag{2.2}$$

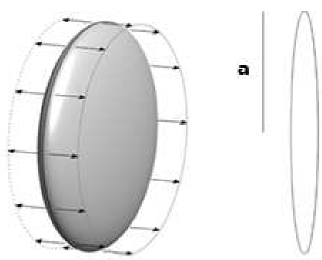

Figure 2.3: A schematic view of a penny shaped-crack of length $L = 2a$. Modified from Davis et al. (2020).

A 3-D penny-shaped crack with elliptical cross-section, filled with a fluid of uniform overpressure δp_0, has the volume: (Tada et al., 2000)

$$V = \frac{8}{3}\frac{1-\nu}{\mu}\delta p_0 a^3 \tag{2.3}$$

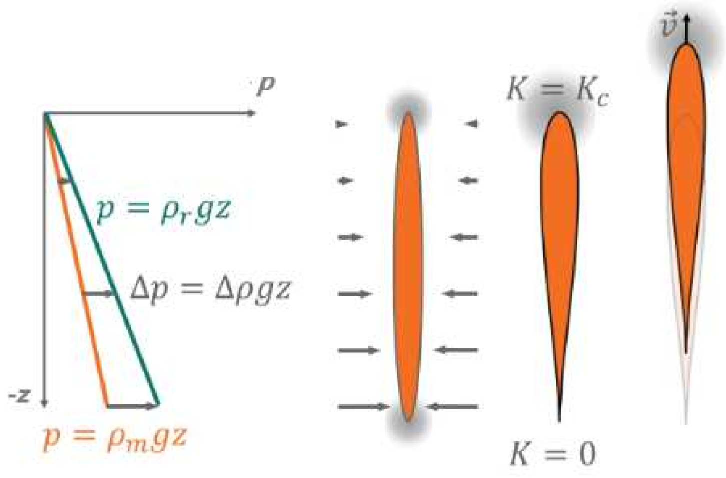

Figure 2.4: Origin of the buoyancy gradient along the fracture. Taken from Rivalta et al. (2024).

A fluid injected in a planar, vertical crack, however, will be subject to a non-uniform overpressure. In fact, lithostatic stress increases more rapidly with depth than hydrostatic stress in the magma (see Fig. 2.4). As a result, the overpressure in the dike decreases with depth, following an approximately linear trend.

As studied by Dahm (2000b) excess pressure at depth z within the fracture is:

$$\delta p(z) = \delta p_0 + \Delta\gamma z, -a \leq z \leq +a \tag{2.4}$$

where δp_0 is the excess pressure at the centre of the fracture, and $\Delta\gamma$ is the overpressure gradient, dp/dz, which, in the case of a vertical crack filled with a fluid of density ρ_m within rock of density ρ_r is $\Delta\gamma = (\rho_r - \rho_m)g = \Delta\rho g$. Cracks that are not vertical have buoyant pressure gradients proportional to the sine of their dip angle δ (Rivalta, 2021).

The linear pressure gradient along the dike profile results in an asymmetric redistribution of the enclosed fluid — more magma will flow towards the region of the fracture which is less pressed from the external stresses. The dike will assume an inverse 'teardrop shape', typical of the Weertman crack.

Due to the fluid redistribution within the dike, the stress intensity factor K at the dike head will be greater than the one at the tail. Within a 3D framework, Davis et al. (2020) showed that the condition $K > K_c$ translates into a condition for the contained volume, V: $V = V_c$. When this condition is met, the fracture head advances, while at the tail the confining pressure squeezes the enclosed fluid, which flows upward. The fracture eventually closes at its back, which translates into the condition $K = 0$. By applying the conditions $K^+ = K_c$ and $K^- = 0$, where the symbols $+$ and $-$ refer to the propagating tip and the tail tip, Davis et al. (2020) retrieves the critical volume for a three-dimensional buoyancy-driven fluid-filled crack dipping by an angle δ (see Appendix A for the full derivation):

$$V_C = \frac{1}{16}\frac{1-\nu}{\mu}\left(\frac{9\pi^4 K_c^8}{\Delta\gamma^5 \sin^5\delta}\right)^{1/3}. \tag{2.5}$$

If the propagation direction, stress gradient and fluid quantity do not change drastically during propagation, the dike will maintain its ability to break rock at the front tip. Hence, the crack will show a self-similar behaviour, with an approximately constant shape and velocity, for great distances. No new influx is needed, so this propagation style is referred to as 'self-driven', or self-sustained. The pressure sustaining dike motion is given by:

$$\Delta p = \int_{-a}^{+a} \frac{d\sigma_n}{dz}\, dz \tag{2.6}$$

As suggested in Davis et al. (2020), some processes that might cause a reduction in volume (e.g., loss of fluid within the dike tail or leaking of fluid into porous rock) may promote dike arrest if they lead to $V < V_c$. It is necessary that any reduction in volume is compensated by variations in the enclosed fluid by other mechanisms (e.g., exsolution of gas in bubbles), as highlighted by Rivalta (2024). If the tail is filled with a viscous fluid, the channel can never completely close (Dahm, 2000a). The quantity of fluid left behind is small for low-viscosity fluids, and a more substantial quantity for high-viscosity fluids.

Estimate of the velocity of propagating fluid-filled fractures

From LEFM, we know that once the condition $K = K_c$ is met for the tip of an 'empty' fracture, then the fracture becomes unstable and propagates fast within the solid. Fluid-filled fractures, however, do not behave in this manner (Rivalta, 2024), as the fluid flow within the fracture needs to 'catch up' before the fracture can propagate further. Time scales of fluid-filled fracture propagation are usually much greater than ones for the propagation of an empty fracture - the latter should theoretically move at the speed of sound in the material (as any dislocation in the continuous, Parfitt and Wilson (2008)), but practically are not as fast. Still a considerable value, however, that made the study of fracture mechanics very impelling to naval engineers whose crafts were continuously hindered by the presence of unstable, dangerous fractures (Rivalta, 2024).

If the fluid is viscous, a pressure drop $\Delta p_{visc} < 0$ within the crack will necessarily develop. If we assume that the gradient of viscous pressure drop over the whole length of the fracture is entirely due to the external stress gradient, then:

$$\Delta\gamma = -\frac{dp}{dz}_{visc} \tag{2.7}$$

This viscous resistance is the physical parameter limiting the rate of fracture propagation. Thus, ascent speed will depend on this quantity. Indeed, driving forces for propagation (i.e., buoyancy) have to overcome resistance forces, which are viscous resistance and fracture resistance (Lister and Kerr, 1991). Once the latter is 'defeated' by opening a propagating fracture, only viscosity of the filling fluid actually controls the ascent of dikes (Watanabe et al., 2002). Given that the physical quantity describing this effect is the viscous pressure drop (or 'viscous drag'), I need to relate it to the propagation velocity of the fracture.

As suggested by Davis et al. (2023), the flow of the enclosed fluid in the fracture may be considered laminar with good approximation - Reynolds number for this problem:

$$Re = \frac{\rho_m 2hv}{\eta} = \frac{\rho_m wv}{\eta} \tag{2.8}$$

is small, typically $<\sim 10^3$.

By assuming a Poiseuille flow, the viscous pressure drop gradient can be expressed as:

$$\frac{dp}{dz}_{visc} = -\frac{3\eta v}{h^2} \tag{2.9}$$

where h is the half-width of the penny-shaped crack, as defined in Section 2.1.

Re-arranging the equation, we obtain an esteem of the ascent speed of the fluid within the fracture (Section 1.3):

$$\bar{v} = \frac{w^2}{12\eta}\Delta\gamma \tag{2.10}$$

in terms of the width $w = 2h$ of the fracture (see Section 2.1), as in Davis et al. (2023).

At this point, it is clear that the fixed volume of injection V should appear as an independent variable in the desired expression, that is, a parameter of the model. Another important factor in controlling dike ascent is the stress gradient (which includes both buoyancy and possibly many other processes), thus also $\Delta\gamma$ may be a useful input parameter. From equation 2.3, one obtains:

$$\delta p_0 = \frac{3}{8}\frac{\mu}{1-\nu}\frac{V}{a^3} \tag{2.11}$$

for the mean internal pressure within the fracture. Since for a penny-shaped crack, equation

$$\delta p_0 = \frac{2}{3}\Delta\gamma a \tag{2.12}$$

holds (see Appendix A), it is simple to obtain that the radius of the crack must be:

$$a = \left(\frac{9}{16}\frac{\mu}{1-\nu}\frac{V}{\Delta\gamma}\right)^{1/4} \tag{2.13}$$

Since the mean aperture of a penny-shaped crack is $w = V/\pi a^2$, the characteristic fluid ascent speed v for a fixed volume $V > V_c$, 3-D fracture can be calculated as (Davis et al., 2023):

$$v_V = \frac{w^2}{12\eta}\Delta\gamma = \frac{4}{27\pi^2}\frac{1-\nu}{\mu}\frac{\Delta\gamma^2 V}{\eta}. \tag{2.14}$$

This represents an estimate for the velocity of a fluid-filled crack of volume V subject to a pressure gradient $\Delta\gamma$. Numerical methods provide more precise solutions, coherent with the approximations used (see, for example, Dahm (2000b)).

The predicted ascent velocity for a vertical magmatic dike calculated by Eq. 2.14 with typical parameter values is of the expected order of magnitude, as shown in Table 2.1.

Quantity	Symbol	Unit	Value
Poisson's ratio	ν	//	0.25
Shear modulus	μ	Pa	$5 \cdot 10^9$
Fracture toughness	K_C	Pa $\cdot\sqrt{m}$	10^8
Fluid/rock density contrast	$\Delta\rho$	kg/m^3	100
Magma viscosity	η	Pa $\cdot$ s	50
Critical volume of propagation	V_C	m^3	$2.1 \cdot 10^6$
Ascent velocity	v_V	m/s	0.76

Table 2.1: The critical volume of propagation was calculated with Eq. 2.5. According to Davis et al. (2020), magma propagation volumes at Piton de la Forunaise volcano observed between 1998 and 2016 range from 0.05 - 3.2 $\cdot 10^6$ m^3. The ascent velocity for a vertical crack was obtained from Eq. 2.14. The result is in agreement with the seismically-inferred values reported at the beginning of this Chapter.

2.2 Interactions with the stress field generated by topographic loading / unloading

In addition to buoyancy, other stress gradients normal to the dike may be present and hence contribute to dike propagation and ascent speed. In particular, surface loads may result in a heterogeneous stress field at depth. This in general results both in inclined dike trajectories and pressure gradients developing along the dike profile. The problem of which pathways a dike will follow during its ascent is then crucial to determine what forces are acting on it.

The effect of surface topography on magma transport within the lithosphere has been investigated by numerical and analogue experiments with air-filled fractures in gelatin (see, for example, Dahm (2000a) or Watanabe et al. (2002)). In particular, the effect of a topographic loading on the free surface was analysed for its evident geophysical relevance. Dike trajectories were seen to deviate and follow - as expected - the most compressive stress axis, which is no longer vertical in these settings, but points towards the load. Thus, dikes that originated at depth are attracted towards the centre of the topographic load (see, for example, Fig. 2.5 and Fig. 2.6).

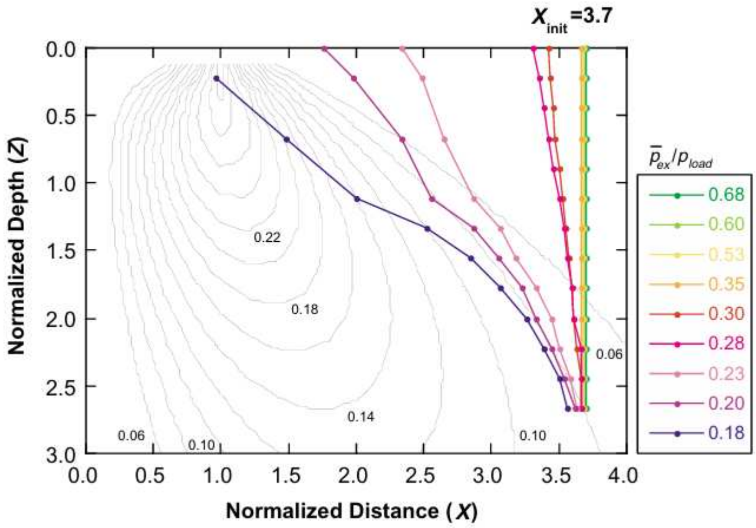

Figure 2.5: The observed paths of a crack upper tip in Watanabe et al. (2002) experiments with air-filled fractures in gelatine. The depth and the distance are normalized by the half width of the load (45 mm). Trajectories are steered depending on the ratio between their excess pressure $\bar{p}_{ex}$ and the loading pressure (kept constant) p_{load}.

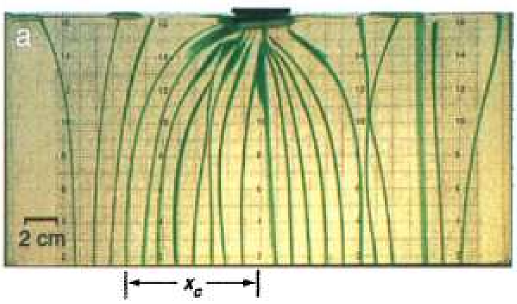

Figure 2.6: Taken from Muller et al. (2001). After completion of the experiment, with propagation paths dyed green to highlight the trajectories of the buoyant air-filled dikes in gelatine.

In fact, the effect of a topographic load is to rotate principal stress axes (Rivalta et al., 2015), hence influencing dike trajectories and causing an accumulation of fluid in some regions or affecting the locations where fluid injections are most likely to reach the free surface. This is especially true at shallow crustal levels, where stresses from the volcanic edifice may overcome regional stresses (Watanabe et al., 2002).

Since the exerted compression by a load will be highest at shallow levels and taper off at depth, if the z axis points upwards ascending dikes will experience a positive gradient of normal stress while reaching for the loading edifice Rivalta (2024).

This gradient acts against the driving force of ascent, since it counterbalances negative buoyancy with respect to the surroundings. Thus, when

$$\Delta\gamma = -\Delta\rho g + \frac{d\sigma_n}{ds} = 0 \tag{2.15}$$

the magma-filled crack will cease to ascend, as pointed out by Watanabe et al. (2002). When this happens, dikes get stalled and emplacement occurs. Thus, topographic loading also controls the depth of emplacement (see Fig. 2.7).

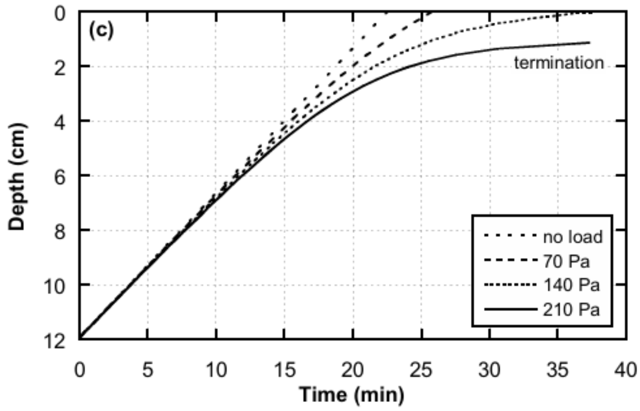

Figure 2.7: The calculated vertical ascent of an air-filed crack tip in gelatine under the influence of a surface load, at $x = 0$, as a function of time. A greater load determines an earlier termination for dike propagation. Taken from Watanabe et al. (2002).

The depth of emplacement of a vertical dike determined by a topographic load modelled as a 2-D strip (cfr. Section 1.2), at the very centre of the load ($x = 0$), is calculated by Watanabe et al. (2002) as:

$$\left.\frac{d\sigma_n}{ds}\right|_{x=0} = \left.\frac{d\sigma_{xx}}{dz}\right|_{x=0} \rightarrow -\Delta\rho g + \frac{4P}{\pi a}\frac{1}{\left[1+\left(\frac{z}{a}\right)^2\right]^2} = 0 \tag{2.16}$$

From this equation, it is clear that higher mountain loads cause deeper emplacement depths for ascending dikes underneath. Unless a great reduction in density occurs, e.g.

by bubble production, the buoyancy cannot propel further the dike. Numerical examples are present in Fig.2.8 - typical values obtained by (Watanabe et al., 2002) for the depth of emplacement are around $\sim 3-5$ km.

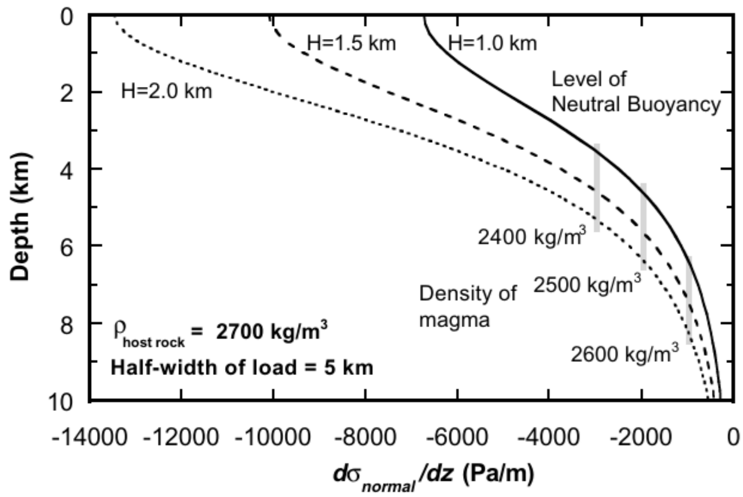

Figure 2.8: Vertical profile of the gradient of normal stress induced by a mountain load modelled as a strip loading, at $x = 0$. The Level of Neutral Buoyancy represents the depth of emplacement for dikes. Taken from Watanabe et al. (2002).

In this way, most dikes with similar size tend to get arrested at similar depth levels under volcanic edifices (Rivalta, 2024). Also Pinel and Jaupart (2000) studied the influence of the gravitational stress on magma ascent and showed that a volcanic edifice can work as a magma filter that prevents the eruption of dense magmas (Watanabe et al., 2002).

Thus, the specific arrangement of eruptive fissures and vents is heavily influenced by the shape of a volcano's edifice. In a cone-shaped loading scenario, the compressive stress at the summit is greater than in lower area below the volcano flanks (Rivalta, 2024). Thus, dikes that manage to overshoot across the depth of emplacement by a reduction in relative density will propagate laterally down the flanks of the edifice. This results in a radial pattern of vents in relation to the volcano's axis, sometimes at considerable distances from the summit.

At calderas, we observe distinctive spatial configuration of vents. The principal stress axes are affected by topographic unloading, that is, removal of a substantial mass, so that they 'flip' their orientation compared to the stress orientation induced by a load - the direction of the most compressive stress axis, σ_1, becomes the orientation of the least compressive stress axis, σ_3, and viceversa (Rivalta, 2024). In this case, ascending dikes are steered away from the centre of the volcano. This results in a bowl-shaped arrangement for intrusions beneath the caldera, resulting in a circumferential pattern for eruptive vents. These may be partly located intra-caldera, and partly located beyond the caldera rim instead. Thus, the stress field at caldera acts as a sort of 'stress barrier', as it traps ascending magmas as horizontal intrusions.

The radial pattern due to edifice loading and the circumferential pattern due to caldera unloading are both present at Fernandina volcano, see Fig. 2.9.

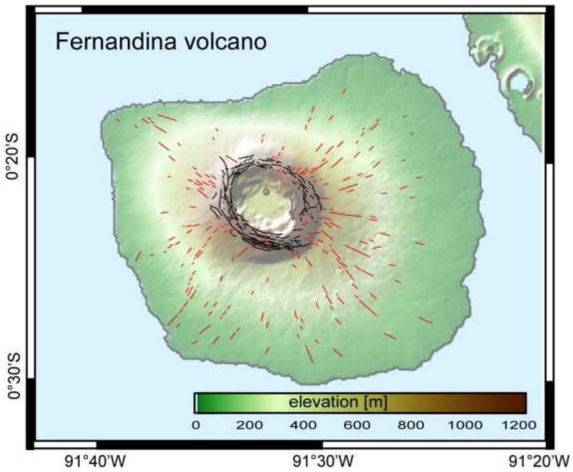

Figure 2.9: Relief map of Fernandina with color-coded elevation. Circumferential and radial fissures are highlighted by the black and red solid lines, respectively. Taken from Corbi et al. (2015).

Dike trajectories for the case of volcanic edifices have been studied by Dahm (2000a) and Maccaferri et al. (2011), while Corbi et al. (2015) and Corbi et al. (2016) analysed propagation of dikes in calderas.

Chapter 3

Testing the model against some real diking events

As presented in the previous Chapter, magma can ascend through the Earth's crust along vertical, but also inclined, pathways, depending on the stress state at depth. An important factor to take into account for many volcanoes creating a heterogeneous stress field are surface loads or unloading. Two archetypical scenarios are, respectively, 'stratocones' and calderas. A stratocone, also known as a stratovolcano, is a type of volcano characterized by a steep, near-conical shape formed from layers of frozen lava, tephra (volcanic ash, rocks, and fragments), and volcanic debris. Examples of stratocones are Mt. Etna and Vesuvius. As seen in Section 2.1, ascent velocities depend on the tilt of the trajectory and the gradient in external stress. It may be interesting to combine the pathway models, firstly, for the case of a stratocone and, secondly, for a caldera, and quantify the typical ascent velocities.

The determination of a dike's ascent velocity is challenging for the following reasons:

1. The time needed for a dike to ascend depends on its ascent velocity. This informs us on approximately when the eruption will take place.

2. The ascent velocity determines the strain rate of rocks, stressed by the dike transiting by, thus influencing the energy release during deformation (whether it is seismic, if strain rates are elevated and rocks respond in a brittle fashion even if they are hotter, or aseismic).

3. Finally, the ascent velocity, determines what geochemical transformations may occur in the ascending magma (variations of p and T in the magma create new equilibra between minerals and dissolved volatiles, with some transformations being favoured, but these need time to occur)

In this Chapter, I develop a simple dike propagation model involving calculation of the velocity of a dike along a tilted trajectory in the stress field induced by a stratovolcano

(Mt. Etna) and a caldera (Campi Flegrei). More specifically, I verify, with application to the two Italian volcanoes, how the stress field induced by different topographic loads and magma buoyancy affect the ascent velocity of magma on different pathways.

I formulated the following procedure: (see MatLab code in Appenix B)

1. I initialise physical parameters (geometry of the loading/unloading, with lateral half-extent a and vertical dimension h, tectonic stress σ_{tec}, rock density ρ_r, magma density ρ_m, magma viscosity η) relevant for my two case studies; these are printed out at the end of the simulation along with the results.

2. I create a 2-D grid of points on the (x, z) plane; note that the z coordinate is positive upward.

3. The stress tensor due to the presence of loading/unloading is computed at every point of the grid. Then, a tectonic component (-5 MPa for Etna, -3.5 MPa for CF) is added. I use the convention of positive compressive stresses.

4. The stress tensor is diagonalised at every point of the grid. The principal stresses (σ_3 and σ_1 are, respectively, the least and most compressive stresses) and their directions are computed by finding at every point the eigenvalues and eigenvectors of the stress tensor. The dike pathway will follow the σ_1 axis, while the driving pressure gradient and velocity will depend on the orientation of the σ_3 axis and its intensity.

5. The gradient of the normal stress (σ_3) is computed at every point in the grid, by a discrete difference between adjacent values; the boundary are excluded to avoid any numerical flaw.

6. the buoyancy pressure gradient is computed at every point in the grid, considering the dike tilt angle if the dike (i.e. σ_1) is not vertical.

7. Once a starting point is chosen for dike nucleation, the program computes the trajectory by following σ_1 at each iteration. Velocity along the points of the trajectory is calculated by Eq. 2.14.

   If the analytical 2-D pathway is parametrised by its arc length s, then I have obtained a discretized version of $v = v(s) = \frac{ds}{dt}$.

8. I derive a timescale estimate for the intrusion. At every point in the trajectory the program computes $dt = \frac{1}{v(s)} ds$, where ds is the increment in the trajectory. The entire path corresponds to a time:

$$T = \int_{s_i}^{s_f} \frac{1}{v(s)} ds \tag{3.1}$$

The time T can be used as a useful parameter to answer the impelling question of when an eruption may occur (provided the dike erupts rather than getting trapped at depth), once the first signs are detected.

9. I also estimate the average ascent speed during the entire intrusion pathways as:

$$\bar{v} = \frac{L}{T} = \frac{1}{T}\int_{s_i}^{s_f} ds \tag{3.2}$$

We recall that the dike pathway is usually inferred from seismic data, while the volume of the intrusion is available from geodetic measurements.

In Section 3.1, I apply my model to Mt. Etna in Sicily, estimating the depth of emplacement of magmatic dikes under the strong topographic load beneath the large volcanic edifice. To do so, I identify at what vertical point along the path the ascent velocity vanishes. In Section 3.2, I finally apply my method to the Campi Flegrei caldera.

3.1 Numerical simulation for a propagating dike below Mt. Etna

With its nearly interrupted volcanic activity, Mount Etna is one of the best monitored volcanoes in the world. Much of the current volcanism at Etna volcano consists of: (1) vertical ascent, followed by lateral movement of magma, radiating from the central conduit down the flanks (Battaglia et al., 2011); (2) from about 2011, intense lava fountain activity at two of the several summit craters of the volcano. I concentrate on deep activities, as my stress models are simplified and I cannot propagate dikes within the volcanic edifice.

The plumbing system of Mt. Etna has been studied over the last decades and constrained by petrological and geophysical data, which suggest magma ascent from a depth of almost 30 km (Palano et al., 2024). Magma reservoirs at Mt. Etna are ephemeral: modelling of ground deformation data and magma geochemistry suggest that reservoirs at different depths activate during different epochs. It is not clear whether different reservoirs form and freeze repeatedly over the course of decades.

Magma propagating from great depth may be affected by the extraordinary topographic load, which is well-approximated by a cone-shaped edifice. The external stress gradient acts against buoyancy to hinder further propagation, and dikes may stall at a specific emplacement depth controlled by the load of the volcano and magma buoyancy.

By simulating the dike pathway under a triangle-shaped load, I find that ascending dikes become trapped in a region at $\sim$ 10 km depth where their velocity becomes approximately zero. I test the scenario assuming different density values for the magma.

Inputs to my simulation are shown in Tab. 3.1 and Tab. 3.2, while results are presented in Tab.3.3. For the dike pathway illustrated in Fig. 3.1, I obtain the time-dependent depth illustrated in Fig. 3.2 and Fig. 3.3. The dike starts to slow down significantly at depth around 12 km, and becomes arrested at depth of 10 km below sea level. The dike velocity steadily decreases along the pathway, with a visible deceleration (Fig. 3.4), as the effect of the topographic load becomes progressively more dominant over buoyancy driving the crack.

Physical quantity	Value	Unit
Edifice radius	15	km
Edifice height	3.3	km
Tectonic (regional) stress	-5	MPa
Lithospheric rock density	2700	kg/m^3
Magma density	2500	kg/m^3
Magma viscosity	30	Pa·s

Table 3.1: Physical quantities for the simulation.

Physical quantity	Value	Unit
Volume of dike intrusion	$2 \cdot 10^6$	m^3
X-coord location of dike nucleation	18	km
Z-coord location of dike nucleation	-20	km

Table 3.2: Input parameters for the simulation: volume injection and trajectory starting point.

Physical quantity	Value	Unit
X-coord location of dike emplacement	11.4	km
Z-coord location of dike emplacement	-9.7	km
Time from start to end of propagation	$4{\cdot}10^3$	h
Time from start to end of propagation	167	d
Average ascent velocity	0.0031	km/h

Table 3.3: Output results of the simulation: location of dike emplacement, total time of propagation with an average ascent velocity.

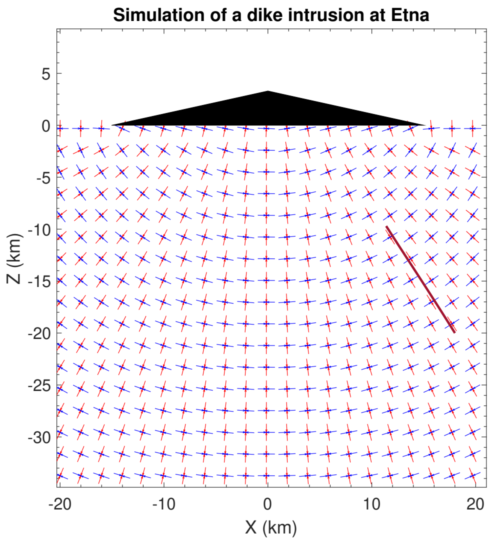

Figure 3.1: Simulation of dike propagation at Etna, with input parameters defined in Tab. 3.1 and Tab. 3.2. The dike gets stalled at the depth of emplacement. Direction of the maximum compressive stress is marked by red arrows; direction of the minimum compressive stress is marked by blue arrows.

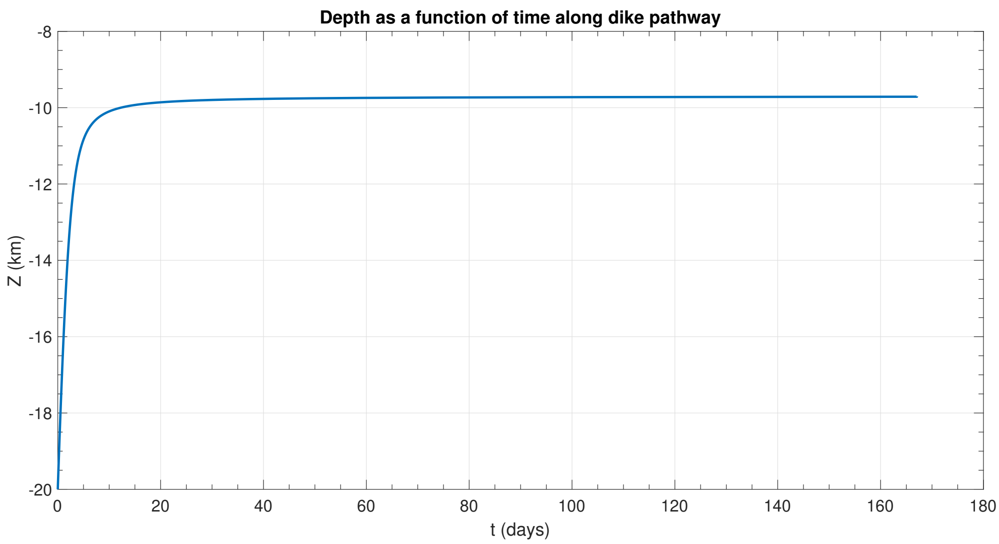

Figure 3.2: Simulation of dike pathway at Etna.

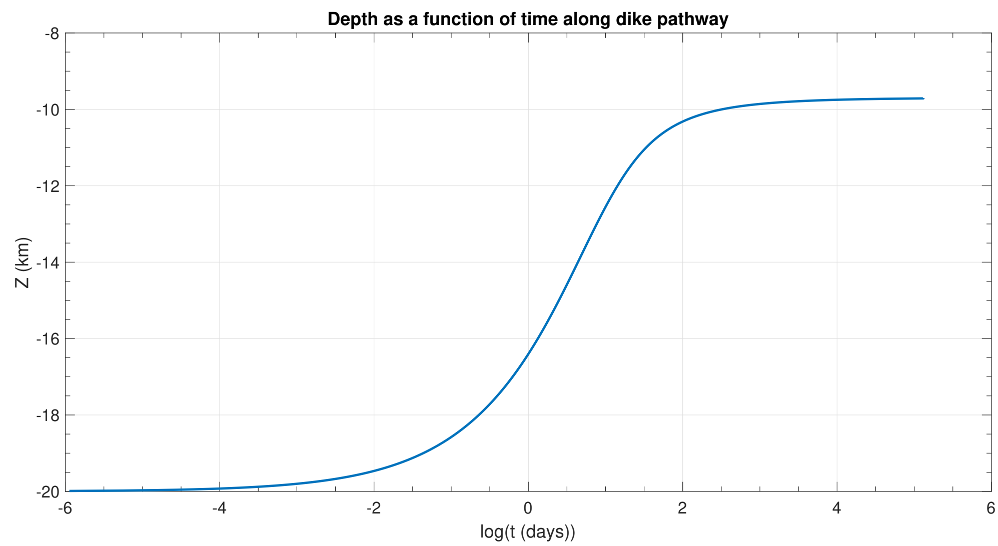

Figure 3.3: Simulation of dike pathway at Etna. Time in days is plotted in logarithmic scale.

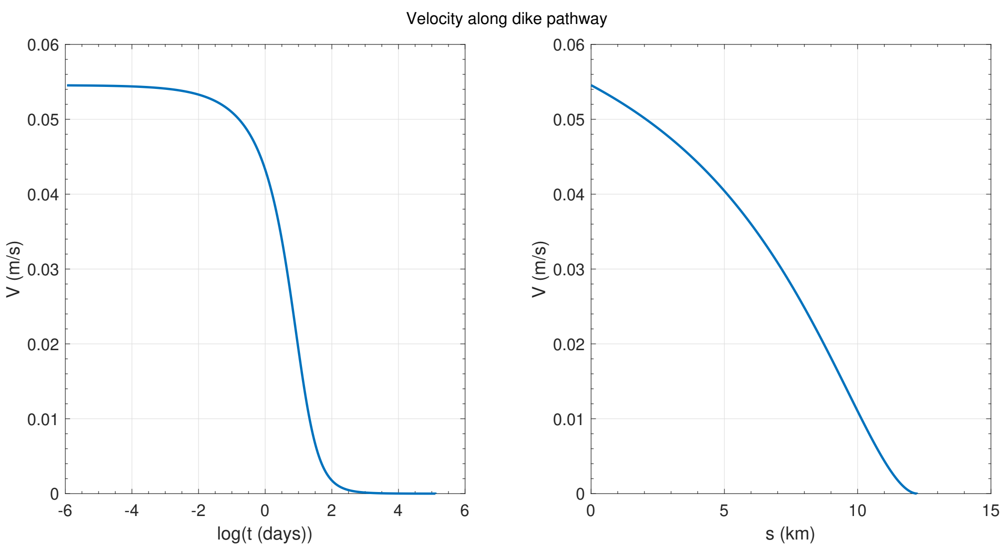

Figure 3.4: Simulation of dike pathway at Etna. Ascent velocity is plotted as a function of the days from the beginning of propagation (left) and as a function of the travelled length (right).

Next, I considered magmas of different buoyancy. In particular, I carried out simulations using different density values:

$$\rho = 1800\,\mathrm{kg/m^3}$$
$$\rho = 2200\,\mathrm{kg/m^3}$$
$$\rho = 2500\,\mathrm{kg/m^3}$$

Dikes with lower buoyancy get stalled at greater depth, as expected (see the results by Watanabe et al. (2002) in Fig. 2.8): for $\rho = 2200\mathrm{kg/m^3}$, the stalling depth is about 7 km, while for $\rho = 1800\mathrm{kg/m^3}$, dikes stall at about 4.5 km (Fig. 3.5). Dike velocities are in the range of geophysically-inferred values (Fig. 3.6 and Fig. 3.7), with a rapid deceleration occurring when the dikes enter into the zone of influence of the load, at radial distance from the base of the volcano of about 1 basal diameter of the volcano edifice.

Depth as a function of time (Fig. 3.14) can be compared to the result of Watanabe et al. (2002) in Fig. 2.7. They found that propagating analog fractures stop when get close to the base of the load, as dikes of different buoyancies in my simulation.

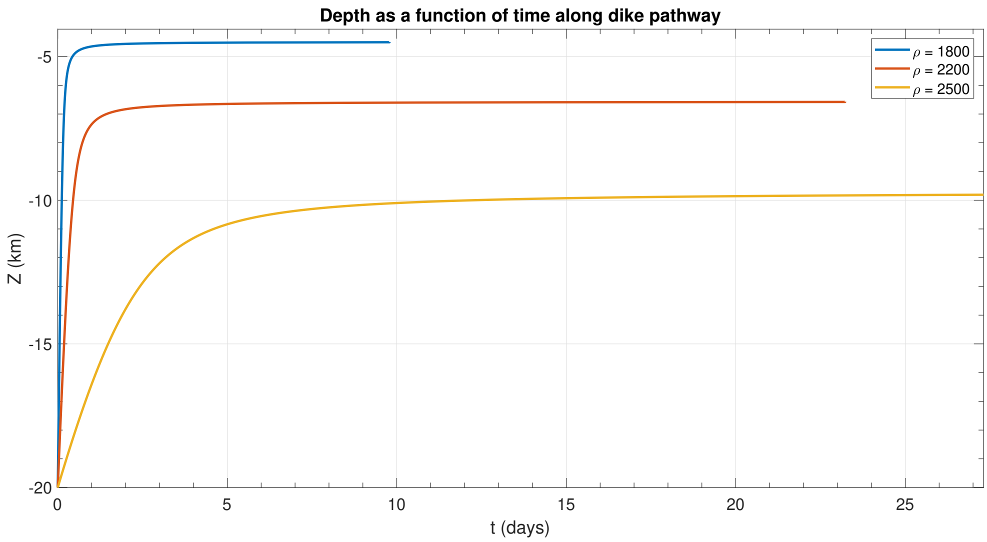

Figure 3.5: Simulation of pathways at Etna for dikes filled with magmas of different density. Density is measured in $\mathrm{kg/m^3}$.

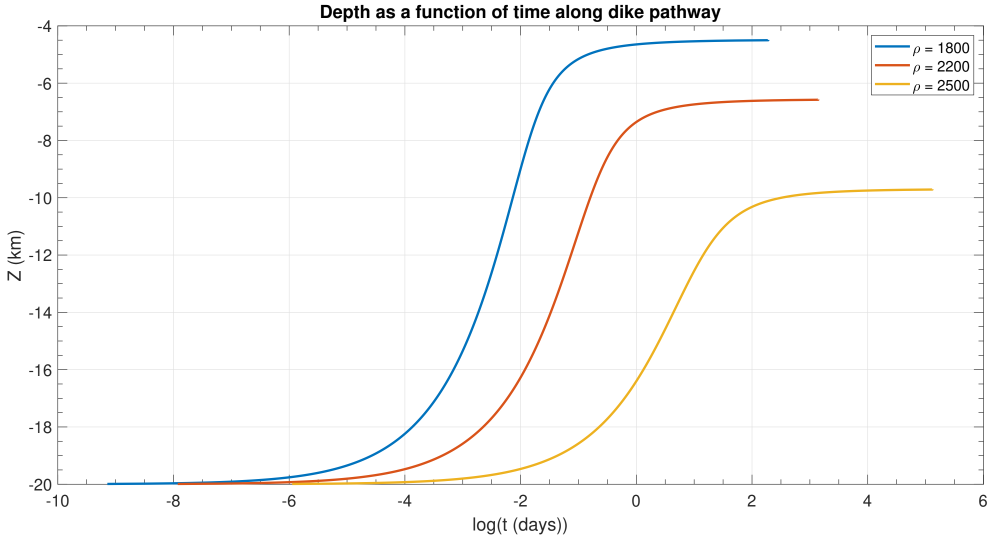

Figure 3.6: Simulation of pathways at Etna for dikes filled with magmas of different density. Density is measured in kg/m^3.

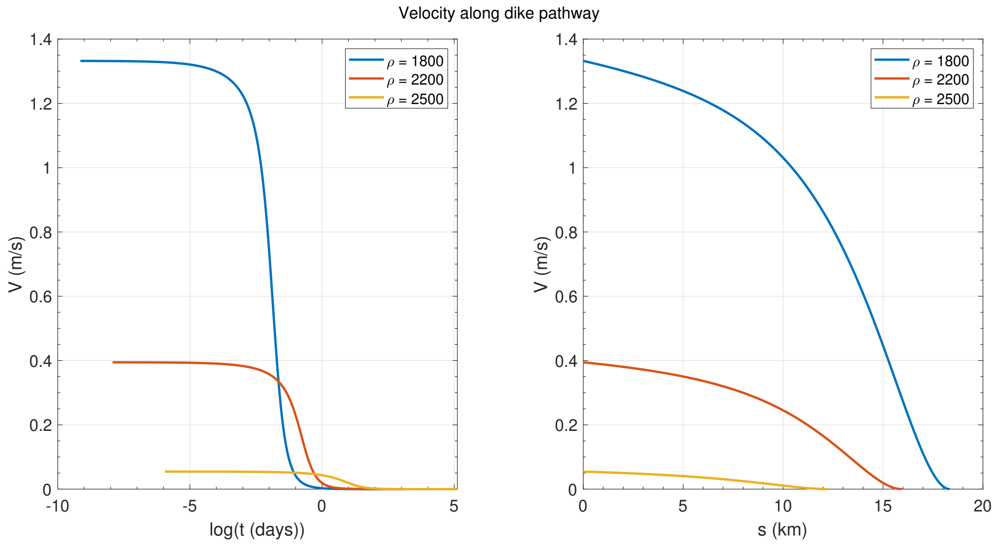

Figure 3.7: Simulation of pathways at Etna for dikes filled with magmas of different density. Density is measured in kg/m^3. Ascent velocity is plotted as a function of the days from beginning of propagation to emplacement (left) and as a function of the travelled length (right).

My result is in agreement with the formation of magma chambers at different depths below Mt. Etna. Magma chambers may form after repeated intrusions of similar magmas accumulating at the same depth, as suggested by modelling of deformation data in the years 2000 and 2001 (see Fig. 3.8), where inflation and deflation sources feeding volcanic activity were located at depths between 5 and 8 km, while sources feeding the current lava fountain activity are located about 1 km below sea level (see Fig. 3.9). A correct assessment of magma sources underneath the main edifice is crucial to evaluate the hazard posed by this volcano and to better understand the dynamics of shallow magma transport.

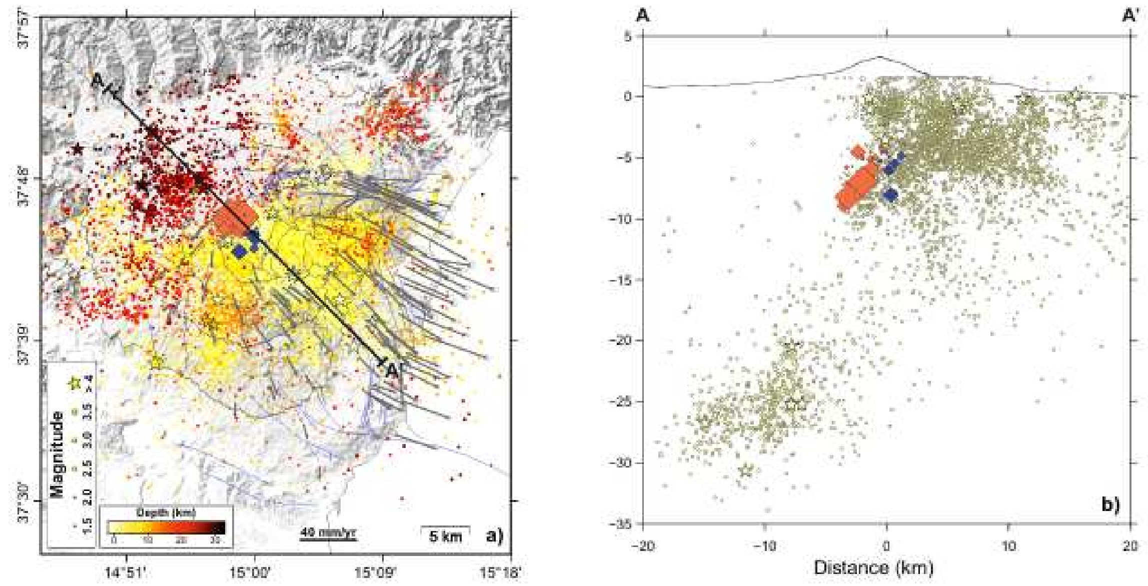

Figure 3.8: Map of Mt. Etna (left: aerial view, right: cross-section), with seismicity ($M > 1$) occurring in the January 2000 - April 2021 period (events with $M > 3.5$ are reported as stars) and the modelled sources of deformation. Taken from Palano et al. (2024).

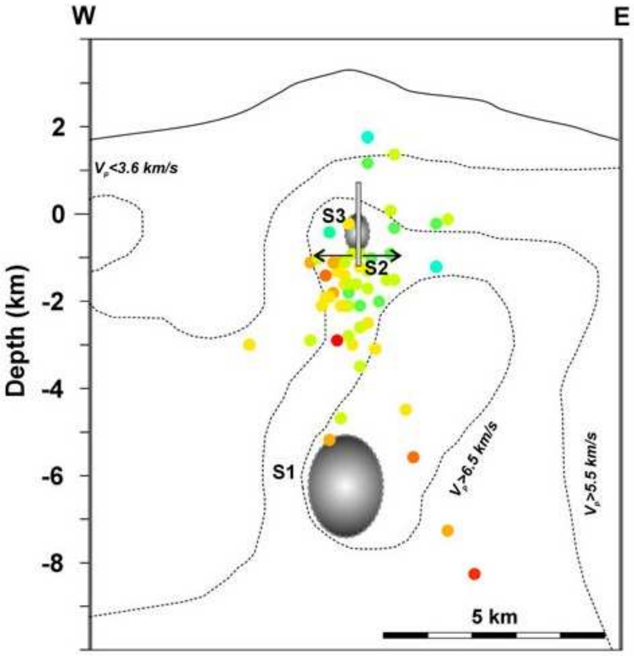

Figure 3.9: W-E section of Etna and different sources. S1 is the classic intermediate storage ($z \sim 6 \pm 2$ km) modelled several times during the prolonged recharging periods over the last 40 years. S3 is the source connected to the events of the lava fountain sequence. Modified from Bonaccorso et al. (2021).

3.2 Numerical simulation for a propagating dike at Campi Flegrei caldera

Campi Flegrei caldera is a large, shallow caldera, with a diameter of roughly 15 km and a depth of about 300 m (Rivalta, 2024). After the main caldera-forming events (see Introduction), post-caldera volcanism developed more than 70 monogenic vents focused predominantly in the North-East sector of the caldera, presently onshore (Davis, 2021), as shown in Fig. 3.10.

Despite the current large uncertainties on what to expect from a possible upcoming magmatic eruption, we have historical accounts of the last one, which occurred as recently as 1538. Guidoboni and Ciuccarelli (2011) collected a reliable archive of historical sources coeval to the so-called Monte Nuovo eruption, this is highly informative also on what to expect as precursory signals to a future possible eruption.

As suggested by Di Vito et al. (2016), ground uplift was present since the end of the 14th century. This increased quite steadily from 1400 to 1536, reaching values in the

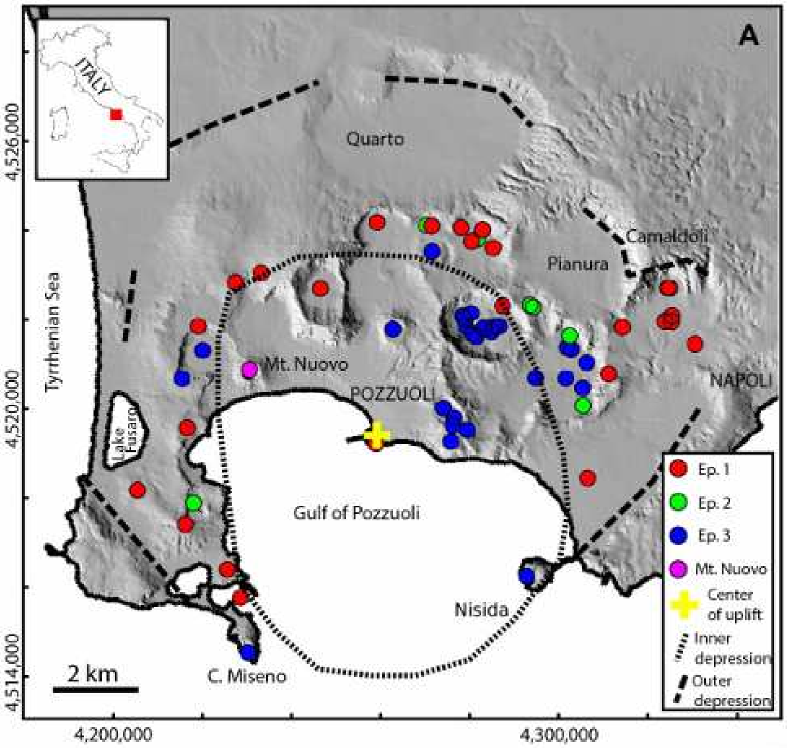

Figure 3.10: Map of the CF caldera with location of vents, colour-coded according to the eruptive history during the last 15 ka. Taken from Rivalta et al. (2019).

order of cm/year. Such an uplift of the caldera floor meant that also the coastal strip emerged, especially at the Pozzuoli area, which is located at the centre of the caldera. Since the end of the 15th century this uplift was accompanied by strong seismicity, that affected also the near city of Naples. From historical records presented in Guidoboni and Ciuccarelli (2011), we know that around 30 h before the eruption also the seabed raised considerably, with water flowing away and an enormous quantity of fish remaining in the shoal. A maximum value of 18.8 m in ground uplift in the future vent-opening area of Monte Nuovo (Di Vito et al., 2016) was reached. After a crack opened at 18.30 of 29th September, eruptive activty from the newly-opened vent continued, with decreasing periods and resumptions, until 17th October, with seismicity carrying on for decade-longer periods.

Monte Nuovo eruption hit locations distant from previous vents. Such eruptions would have been hard to anticipate (Rivalta et al., 2019), even today, if we relied upon the exclusive use of probability maps.

Currently, the caldera presents a net uplift of more than 1 m at the caldera centre since 2012, after a period of subsidence. Such large deformations inevitably produce earthquakes. These earthquakes, thus, are rather a natural response of lithospheric rock to the extreme strain, and no direct evidence is available to correlate them to any uprising of magma.

A possible explanation for the current deformation may be the following. A magma influx is present somewhere at depth, and magmas contain dissolved volatile components. As the magma is decompressed during ascent or as it stalls at shallower depth, the volatile solubility decreases, leading to a separation of the gaseous phase. The exsolved gases rise through a porous hydro-thermal system located above the magmatic system. These fluids within the hydro-thermal region are thus responsible for the uplift.

As magma is transported towards the surface in a dike, as during the Monte Nuovo eruption, we expect a deviation from radial symmetry of deformations, since magma intrusions are sheet-like and may strongly affect the pattern of deformation.

In my simulation, the caldera is modelled, in plane strain, as a rectangular excavation lacking significant loading topography. The unloading is calculated with an effective depth $h^{eff} > h$ for the caldera, which accounts for the density of sediments which only partially compensate for the missing crustal rocks after caldera collapse (Mantiloni et al., 2024).

I adapted the parameters of the unloading in such a way that a trajectory departing from a magma chamber at depth $z = -4$ km, from a location offset by $x = 1$ km from the caldera centre, reaches the surface at the Monte Nuovo location (ca. 3.3 km radius distance from the centre). This was indicated by Rivalta et al. (2019) as the most likely 'radius' for future vents at CF.

Inputs to my simulation are shown in Tab. 3.4 and Tab. 3.5, while results are presented in Tab.3.6. For the dike pathway illustrated in Fig. 3.11 with a solid red line, I obtain the time-dependent depth illustrated in Fig 3.12. While ascending dikes at Mt. Etna were strongly decelerated, for the CF caldera dikes present a steep increase in their ascent velocity while reaching for the Earth's surface (Fig. 3.13). Acceleration is due to the dike being progressively more buoyant, as the pathway in the last few kms under the surface is almost vertical, as shown in Fig. 3.11.

Physical quantity	Value	Measurement unit
Caldera radius	7.5	km
Excavation depth (efficient)	0.3	km
Tectonic (regional) stress	-3.5	MPa
Lithospheric rock density	2600	kg/m^3
Magma density	2200	kg/m^3
Magma viscosity	1000	Pa·s

Table 3.4: Physical quantities for the simulation

I also determine the pathway of an ascending dike nucleating from a hypothetical

Physical quantity	Value	Measurement unit
Volume of dike intrusion	$250 \cdot 10^6$	m^3
X-coord location of dike nucleation	1	km
Z-coord location of dike nucleation	-4	km

Table 3.5: Input parameters for the simulation: volume injection and trajectory starting point

Physical quantity	Value	Measurement unit
X-coord location of eruption	3.4	km
Z-coord location of eruption	0.0	km
Time before eruption	12	h
Time before eruption	0.52	d
Average ascent velocity	0.41	km/h

Table 3.6: Output results of the simulation: location of eruption, total time of propagation with an average ascent velocity.

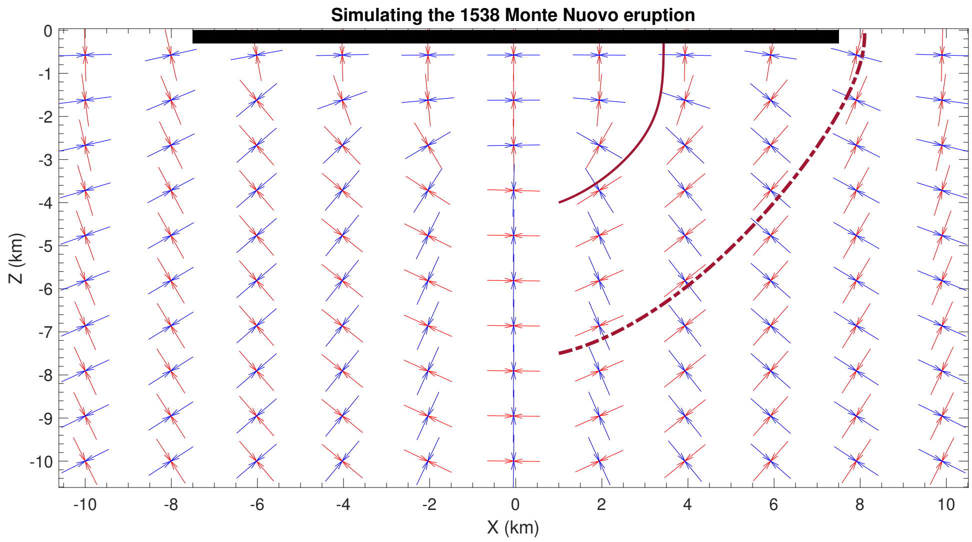

Figure 3.11: Simulation of dike propagation at CF, with input parameters defined in Tab. 3.4 and Tab. 3.4. Continuos line shows the simulated trajectory of the dike responsible for the Monte Nuovo Eruption; the dashed line shows the trajectory of a dike nucleating from greater depth and erupting outside the caldera. Direction of the maximum compressive stress is marked by red arrows; direction of the minimum compressive stress is marked by blue arrows.

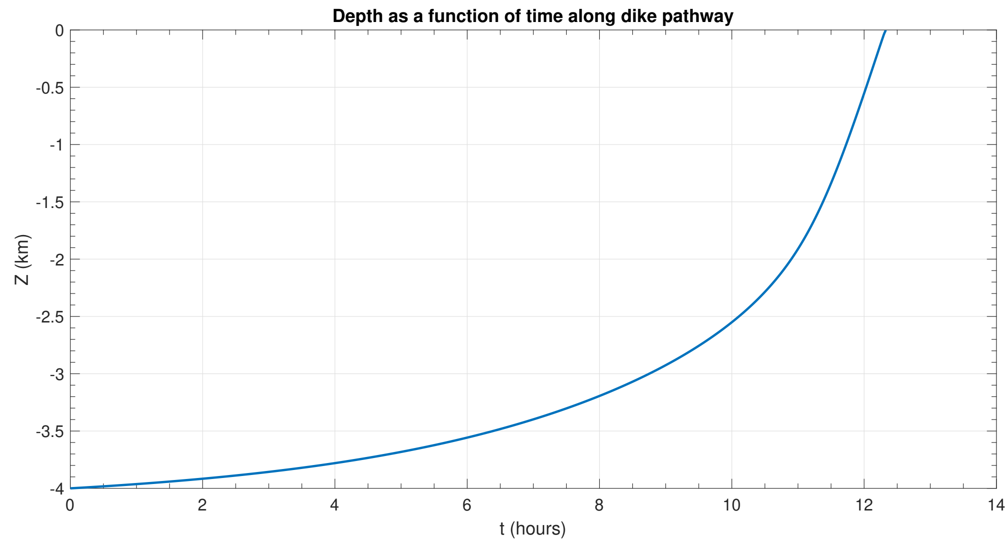

Figure 3.12: Simulation of dike pathway at CF.

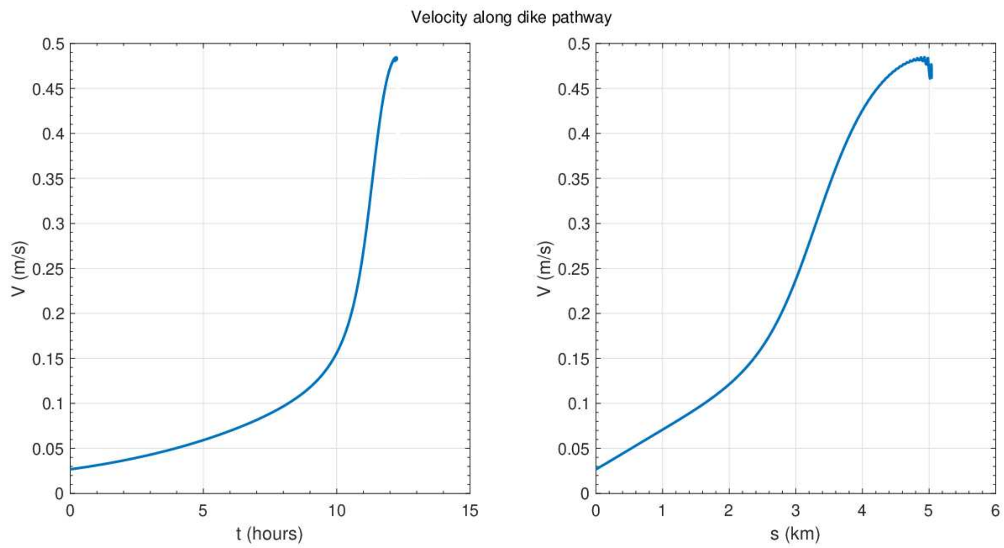

Figure 3.13: Simulation of dike pathway at CF. Time in hours is plotted in logarithmic scale.

magmatic source at greater depths. As seen in Fig. 3.11, intra-caldera eruptions are possible only for dikes at shallower depths, such as the -4 km case.

The timescale of dike ascent is also in agreement with historical data, remarking strong seismicity at about 12 hours before the eruption.

Next, I consider the effect of magmas of different buoyancy filling the dikes (see Fig. 3.14 and Fig. 3.15.). In particular, I carry out simulations using the following densities:

$$\rho = 1800\,\mathrm{kg/m^3}$$
$$\rho = 2200\,\mathrm{kg/m^3}$$
$$\rho = 2500\,\mathrm{kg/m^3}$$

I find that more buoyant dikes ascend more rapidly beneath the caldera, as expected. In addition, dikes tend to accelerate after travelling about 2.5 km, i.e. when their trajectories become increasingly vertical.

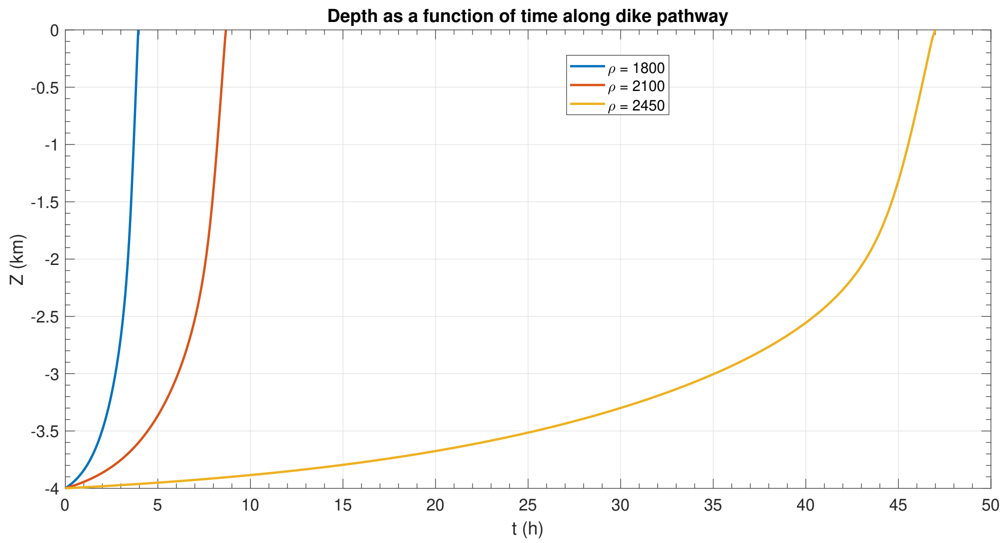

Figure 3.14: Simulation of pathways at CF for different buoyant dikes. Density is measured in $\mathrm{kg/m^3}$.

In conclusion, predicted ascent velocities for dike ascent beneath the CF caldera suggest a timescale of hours (12 h for a dike with average buoyancy) before an eruption occurs (see Fig.3.15), with dikes accelerating before reaching the surface.

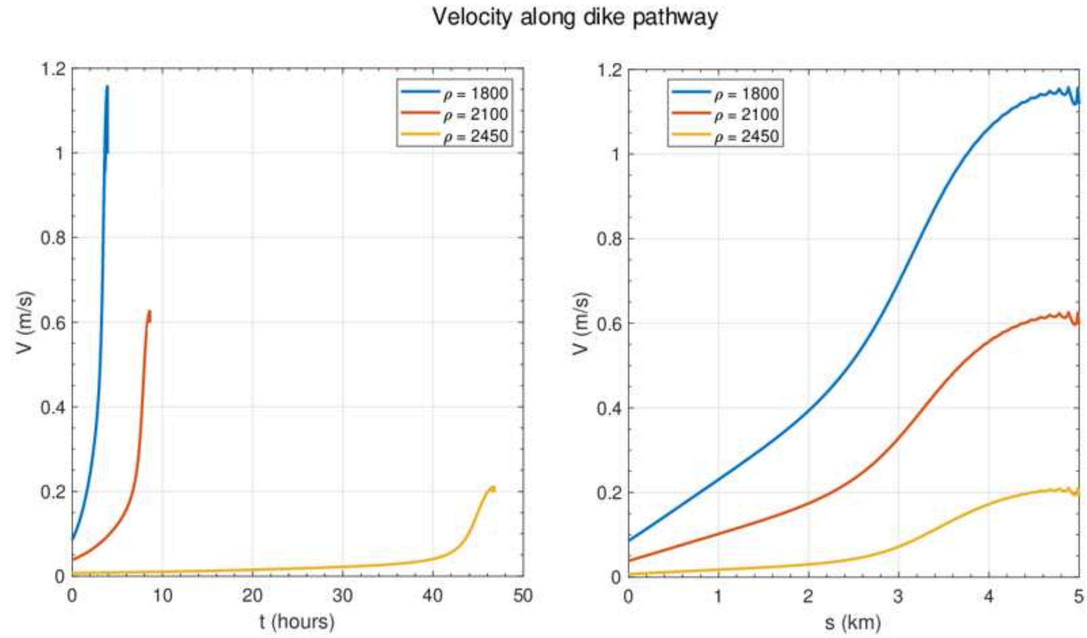

Figure 3.15: Simulation of pathways at CF for different buoyant dikes. Density is measured in kg/m^3. Ascent velocity is plotted as a function of the hours from beginning of propagation to eruption (left), and as a function of the travelled length (right).

Chapter 4

Conclusions

Simulations carried out for CF and Etna achieve encouraging results. In particular, the last eruption at CF (Monte Nuovo, 1538) is simulated with a magmatic dike nucleating from 4 km depth and ascending in a time interval of about 12 hours from beginning to eruption. This value may be used as a quick estimate of the time before another eruptive vent opens at CF, after the geophysical signals related to dike propagation are detected, provided that parameters do not change significantly.

However, this solution carries large uncertainties as it arises from some approximations.

In the first place, the stress state at depth was heavily simplified. In fact, I adopted a plain strain assumption instead of a three-dimensional approach. In addition, the presence of a magma chamber and possibly other magmatic intrusions almost certainly interact with the dike pathway through alterations in the stress field. The magma chamber was neglected also as a possible source of driving pressure for the dike. This effect may be only significant at earlier times, but still may be taken into account.

Phase transitions in the filling fluid are possible due to variations in its thermodynamic conditions. In particular, variations in fluid density $\Delta\rho$ due to bubbles forming inside the fracture may also deplete the magmas of water molecules which has the effect of leading to polymerization of the magmas, favouring a viscosity increase and the nucleation of crystals. These in turn deeply influence the fluid viscosity, impeding fluid flow with an increase in $\Delta\eta$. The volatile component is thus an essential mechanism to be studied in order to successfully model timescales of eruption. Variations in magma density and viscosity that occur during dike ascent influence the ascent velocity and might be taken into account in future studies.

Finally, I neglected heat conduction between the magmatic dike and its surroundings. The timescale of propagation needs to be compared with the timescale of magma solidification. A dike may get arrested in its propagation because of thermal effects, if it freezes underneath the crust. This aspect is more important for high-viscosity magmas. CF magmas are relatively low-viscosity, but they can become much higher viscosity as they ascend and de-volatilise.

Several parameters such as density ρ and viscosity η appear in the considered equation for the ascent velocity. Thus, determining how variations of these quantities within reasonable ranges would affect my results would allow me to estimate how uncertainties on the parameters are propagated by the model onto model results. This can be investigated by e.g. assigning a Gaussian distribution to the parameters ρ and η and then examining the consequent distribution for the values of the velocity. The same reasoning is true for the volume of the magma-batch, although a power-law type of distribution may be well-suited rather than a Gaussian (we expect a great amount of small propagating magma batches and fewer of bigger volumes).

4.1 Future prospects and implementation

Despite its many different simplifications, the method applied to determine the ascent velocity of magmatic dikes along tilted pathway in the lithosphere seems promising. In the future, validation on many other case studies from volcanic eruptions or analog experiments may result beneficial to improve the reliability of my model. The ultimate goal would be to increase its predictiveness towards physical observations, by including the neglected aspects that are most required by real data sets.

Another possible development line could be to compare my model with the coupled pathway-velocity model of Furst et al. (2023), also two-dimensional.

The most compelling priority, however, is expanding the model to compute the 3D trajectory of dikes. Real dikes, in fact, are often seen to deviate away from the initial plane of propagation (see, for example, the 2018 dike propagation at Sierra Negra, Galápagos Islands, described in Davis et al. (2021)). The implementation of such a feature may provide my model with more accurate trajectories, in order to achieve time estimates even for more complex propagation scenarios. This would, on the other hand, require longer computation times. My model allows to rapidly estimate the ascent velocities of propagating magma batches, with a near-analytical approach.

Acknowledgments

I wish to sincerely thank professor Eleonora Rivalta for her immense support and her precious kindness in the creation of this thesis. She carefully provided me with the tools, the delight and the challenges of passionate scientific research.

Appendix A

Analytical determination of a critical volume of injection

In their article, Davis et al. (2020) state that the stress intensity factor for a Mode-I penny-shaped fracture of radius (half-length) a subject to a generic linear stress gradient can be expressed as the superposition of:

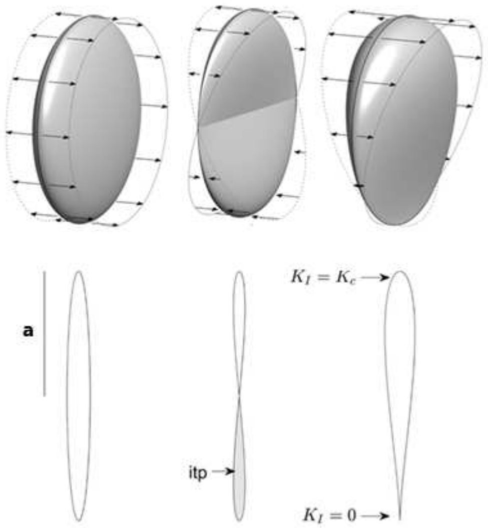

Figure A.1: *Top: Propagating fracture as the superposition of a penny-shaped fracture and a zero-volume crack subject to a linear pressure gradient. Bottom: Cross sections of crack wall displacement, itp =interpenetration. Modified from Davis et al. (2020).*

- K_I for a penny-shaped fracture subject to a uniform pressure at its centre δp_0:

$$K_I = \frac{2}{\pi}\delta p_0 \sqrt{\pi a} \tag{A.1}$$

- K_I for a penny-shaped fracture subject to a linear pressure gradient $\Delta\gamma$ where pressure is equal to 0 at the fracture's midpoint:

$$K_I^{\pm} = \pm\frac{4}{3\pi}\Delta\gamma a\sqrt{\pi a} \tag{A.2}$$

  where + refers to the propagating tip and − to the basal tip, respectively.

To determine an expression for the critical volume of injection, i.e. volume of magma necessary to trigger dike propagation, fracture mechanics is applied to a vertical, penny-shaped crack of width $w = 2h$ ($L = B = 2a$). The condition for fracture growth is related to the stress intensity factors at the head and tail of the dike:

$$K_+ = K_C \tag{A.3}$$

$$K_- = 0 \tag{A.4}$$

Requiring $K_I^- = 0$ results in $\delta p_0 = 2/3\Delta\gamma a$ and thus

$$\delta p^{\pm} = \delta p(z = \pm a) = (2/3 \pm 1)\Delta\gamma a \tag{A.5}$$

Negative pressures in Eq. A.5 are interpreted as the fluid dragging the crack walls behind when propagating upwards. Requiring $K_I^+ = K_C$ and substituting what we have found for δp_0 yields an expression for the pressure gradient:

$$\Delta\gamma = \Delta\rho g = \frac{3}{8}\frac{K_C}{a\sqrt{\pi a}} \tag{A.6}$$

and one for the excess pressure at the centre of the fracture:

$$\delta p_0 = \frac{2}{3}\Delta\gamma a = \frac{K_C}{4\sqrt{\pi a}} \tag{A.7}$$

In addition, rearranging for a yields:

$$a = \left(\frac{3\sqrt{\pi}K_C}{8\Delta\gamma}\right)^{2/3} \tag{A.8}$$

The fracture grows when it reaches a critical value for its volume: Davis et al. (2020) calculates the volume of crack based on the equation for a crack pressurised by uniform pressure δp_0, as the antisymmetric pressure contribution integrates to zero. Thus using Eq. 2.3 combined with Eqs. A.7 and A.8 results in ($\Delta\gamma \rightarrow \Delta\gamma\sin\delta$ if dike is inclined)

$$V_C = \frac{1}{16}\frac{1-\nu}{\mu}\left(\frac{9\pi^4 K_C^8}{\Delta\gamma^5\sin^5\delta}\right)^{1/3} \tag{A.9}$$

According to Davis et al. (2020), this equation requires validation in order to evaluate the bias due to approximating the shape of the propagating crack as circular. They carry out this task by numerical integration.

Appendix B

MatLab script to simulate dike propagation

Here I attach one of the MatLab scripts employed in my simulations. In particular, this code was used to simulate dikes of different buoyancies ascending at CF (see, for example, Fig. 3.15). However, the functioning of the code is similar to all the ones used in this thesis.

```
function [S] = boxload_ZpositiveUpward(x,z,x0,a,nu,P0)

x = x(:);
z = -z(:);

if any(z<0)
    error('Positive Z values: Z must be negative!')
end

% Strip loading from Dahm 2000
th1 = atan2(x-x0+a,z);
th2 = atan2(x-x0-a,z);
sxx = -P0/pi*(th2-th1-0.5*sin(2*th2)+0.5*sin(2*th1));
szz = -P0/pi*(th2-th1+0.5*sin(2*th2)-0.5*sin(2*th1));
sxz = -(-P0/pi*((sin(th2)).^2-(sin(th1)).^2));

syy = nu*(sxx+szz); % plain strain condition

S = [sxx syy szz sxz];


% Parameters
```

```
    % Magma and host rock density
    rho = 2600; %kg m^-3, medium density
    rho_m = [1800 2100 2450]; %kg m^-3, magma density
    % rho_m may change if bubbles are present

    % Elasticity and stress
    g = 9.8; % m/s^2, acceleration due to gravity
    nu = 0.25; % Poisson's ratio
    mu = 30e9; % Pa, medium shear modulus
    Kc  = 200e6; %Pa*m^(1/2), Rock fracture toughness

    Sxx_tec = 0; %Pa, regional stress
    eta = 0; %Pa*s, magma viscosity

    % Load geometry
    X0 = 0; %m, coordinates of load/unload centre
    a = 0; % m, half-width of box
    h = 0; % m, load excavation depth

    % Typical parameter values for CF caldera
    eta_CF = 1e3;
    Sxx_tec_CF = -3.5e6;
    a_CF = 7.5e3;
    h_CF = 0.3e3;

    x_start = 1e3;
    % x-coord of starting point for reference trajectory
    z_start = -4e3;
    % z-coord of starting point for reference trajectory

% Parameters initialisation
    eta = eta_CF;
    Sxx_tec = Sxx_tec_CF;
    a = a_CF;
    h = h_CF;
    P0 = - rho*g*h; %Pa, loading/unloading pressure
    % use (+ loading, - unloading)
    % Positive compressive stress, negative extensive stress.

% Creating a grid of calculation points
    RangeX_i = -10e3;
    RangeX_f = +10e3;
    RangeZ_i = -20e3;
```

```
    RangeZ_f = 0;

     nx    = 202; nz = 192; % Number of calculation points

    x = linspace(RangeX_i, RangeX_f, nx);
    z = linspace(RangeZ_i, RangeZ_f, nz);

    [X, Z] = meshgrid(x, z);

M = numel(X);

S = zeros (M, 4);
[S] = boxload_ZpositiveUpward(X, Z, X0, a, nu, P0);
% this results in a matrix S = [Sxx Syy Szz Sxy]
% in every point of the grid;

% Add tectonic stres
S = S + [Sxx_tec 0 0 0];

Sol = zeros (M, 6);
% initialisation of empty matrix,
% to fill with solution of eigenvalue problem

% Matrix diagonalisation in every point of the grid
for i = 1 : M
    Stress = [  S(i, 1) S(i, 4)
                S(i, 4) S(i, 3) ];
    [EigenVecMatrix, DiagonalMatrix] = eig( Stress );
    % EigenVecMatrix has the components of the
    % three eigenvectors as columns
    % DiagonalMatrix has the thee eigenvalues
    % on the diagonal and 0 otherwise
    Sol(i,:) = [EigenVecMatrix(:)' ...
            DiagonalMatrix(1,1) DiagonalMatrix(2,2)];

    % Use the sort function to put the eigenvalues in ascending order
    % and reorder the corresponding eigenvectors.
    % Find the index of reordered elements:
    [d,ind] = sort(diag(DiagonalMatrix));
    % Use ind to reorder elements (from small to large):
    Ds = DiagonalMatrix(ind,ind);
    % Use ind to also reorder the eigenvectors so that
    % they are correctly associated to the reordered eigenvalues:
```

```
    Vs = EigenVecMatrix(:,ind);

    Sol(i,:) = [Vs(:)' Ds(1,1) Ds(2,2)];
end
% Change sign to all eigenvectors if the z-component
% of the eigenvector of the largest eigenvalue is negative:
Sol(Sol(:,4) < 0, 1:4) = - Sol(Sol(:,4) < 0, 1:4);
% Inconsistency in the "verse" of eigenvectors in a field
% will mess up streamlines plots

Sigma1 = reshape( Sol(:, 6), size(X));
% Sigma1 is the most compressive principal stress
Sigma3 = reshape( Sol(:, 5), size(X));
% Sigma3 is the least compressive principal stress

Autoval1_1 = reshape(Sol(:,3), size(X));
% x component of Sigma1 eigenvalue
Autoval1_2 = reshape(Sol(:,4), size(X));
% z component of Sigma1 eigenvalue
Autoval3_1 = reshape(Sol(:,1), size(X));
% x component of Sigma3 eigenvalue
Autoval3_2 = reshape(Sol(:,2), size(X));
% z component of Sigma3 eigenvalue

trajectory = streamline(X, Z, Autoval1_1, Autoval1_2, ...
    x_start, z_start);
xData = get(trajectory, 'XData');
zData = get(trajectory, 'YData');

%%%%%%%%%%%%%%%%
traj = [xData(1,:); zData(1,:)];
[S_CF] = boxload_ZpositiveUpward(traj(1,:), traj(2,:), ...
    X0, a, nu, P0);

S_CF = S_CF + [Sxx_tec 0 0 0];

M_CF = size(xData);

Sol_CF = zeros(M_CF(2), 6);

for i = 1 : M_CF(2)
    Stress = [ S_CF(i, 1) S_CF(i, 4)
               S_CF(i, 4) S_CF(i, 3) ];
```

```
        [EigenVecMatrix, DiagonalMatrix] = eig( Stress );
        Sol_CF(i,:) = [EigenVecMatrix(:)' ...
                    DiagonalMatrix(1,1) DiagonalMatrix(2,2)];

        [d,ind] = sort(diag(DiagonalMatrix));
        Ds = DiagonalMatrix(ind,ind);
        Vs = EigenVecMatrix(:,ind);

        Sol_CF(i,:) = [Vs(:)' Ds(1,1) Ds(2,2)];
    end
    Sol_CF(Sol_CF(:,4) < 0, 1:4) = - Sol_CF(Sol_CF(:,4) < 0, 1:4);

    Sigma1_CF = reshape( Sol_CF(:, 6), M_CF);
    Sigma3_CF = reshape( Sol_CF(:, 5), M_CF);

    Autoval1_1_CF = reshape(Sol_CF(:,3), M_CF);
    Autoval1_2_CF = reshape(Sol_CF(:,4), M_CF);
    Autoval3_1_CF = reshape(Sol_CF(:,1), M_CF);
    Autoval3_2_CF = reshape(Sol_CF(:,2), M_CF);
    %%%%%%%%%%%%%%

dSigma3_dX_CF = diff([Sigma3_CF(1,:) 0]) ./ diff([xData(1,:) 0]);
dSigma3_dZ_CF = diff([Sigma3_CF(1,:) 0]) ./ diff([zData(1,:) 0]);

dSigma3_ds_CF = dSigma3_dX_CF.*Autoval1_1_CF + ...
                dSigma3_dZ_CF.*Autoval1_2_CF;

DdSigma3_ds_CF = [dSigma3_ds_CF(1,1:end-1) dSigma3_ds_CF(1,end-1)];

for j = 1:size(rho_m,2)

Buoyancy_CF = (rho-rho_m(1,j))*g*Autoval1_2_CF;

D_g_CF = - DdSigma3_ds_CF + Buoyancy_CF;

Vol_CF = 25e6; % m^3, volume of magma batch injected

V_CF = 4/(27*pi^2) * (1-nu)/mu * Vol_CF/eta * ...
        (D_g_CF(D_g_CF > 0)).^2; % m/s, magma ascent speed

invV_CF = 1./V_CF;
STOP = size(V_CF,2);

```

```
dl = diff([xData(1,1:STOP) xData(1,STOP)]) ...
   .* Autoval1_1_CF(1, 1:STOP) + diff([zData(1,1:STOP) zData(1,STOP)]) ...
   .* Autoval1_2_CF(1, 1:STOP);

dt = invV_CF .* dl;

t_cumulative = zeros(1,STOP);
for i = 2:STOP
    t_cumulative(1,i) = t_cumulative(1,i-1) + dt(1,i);
end

l_cumulative = zeros(1,STOP);
for i = 2:STOP
    l_cumulative(1,i) = l_cumulative(1,i-1) + dl(1,i);
end

L = sum(dl);
T = sum(dt);

InputParameters = {
    'Raggio della caldera (km)';
    'Profondit  della caldera (km)';
    'Sforzo tettonico (MPa)';
    'Densit  della crosta (kg/m^3)';
    'Densit  del magma (kg/m^3)';
    'Viscosit  del magma (Pa*s)';
    'Volume of dike intrusion (km^3)';
    'X-coord location of dike nucleation (Km)';
    'Z-coord location of dike nucleation (km)'};
Values = [
    a_CF/1e3;
    h_CF/1e3;
    Sxx_tec_CF/1e6;
    rho;
    rho_m(1,j);
    eta_CF;
    (Vol_CF/1e9);
    xData(1,1)/1e3;
    zData(1,1)/1e3];
InputT = table(Values, 'RowNames', InputParameters);

OutputResults = {
    'X-coord location of eruption (km)';
```

```
    'Z-coord location of eruption (km)';
    'Time in hours';
    'Time in days';
    'Average ascent velocity (km/h)'};
Values = [
    xData(1,STOP)/1e3;
    zData(1,STOP)/1e3;
    T / 3600;
    T / 86400;
    (L/1e3)/(T / 3600)];
OutputT = table(Values, 'RowNames', OutputResults);

disp(InputT)
disp(OutputT)
```

Bibliography

Anderson, E. M. (1905). The dynamics of faulting. *Transactions of the Edinburgh Geological Society*, 8(3):387–402.

Atkinson, C. and Craster, R. (1995). Theoretical aspects of fracture mechanics. *Progress in Aerospace Sciences*, 31(1):1–83.

Battaglia, J., Ferrazzini, V., Staudacher, T., Aki, K., and Cheminée, J.-L. (2005). Pre-eruptive migration of earthquakes at the Piton de la Fournaise volcano (Réunion Island). *Geophysical Journal International*, 161(2):549–558.

Battaglia, M., Di Bari, M., Acocella, V., and Neri, M. (2011). Dike emplacement and flank instability at Mount Etna: Constraints from a poro-elastic-model of flank collapse. *Journal of Volcanology and Geothermal Research*, 199(1-2):153–164.

Beauducel, F., Peltier, A., Villié, A., and Suryanto, W. (2020). Mechanical imaging of a volcano plumbing system from gnss unsupervised modeling. *Geophysical Research Letters*, 47(17):e2020GL089419.

Bonaccorso, A., Carleo, L., Currenti, G., and Sicali, A. (2021). Magma migration at shallower levels and lava fountains sequence as revealed by borehole dilatometers on etna volcano. *Frontiers in Earth Science*, 9:740505.

Cesca, S., Letort, J., Razafindrakoto, H. N. T., Heimann, S., Rivalta, E., Isken, M. P., Nikkhoo, M., Passarelli, L., Petersen, G. M., Cotton, F., and Dahm, T. (2020). Drainage of a deep magma reservoir near Mayotte inferred from seismicity and deformation. *Nature Geoscience*, 13(1):87–93.

Corbi, F., Rivalta, E., Pinel, V., Maccaferri, F., and Acocella, V. (2016). Understanding the link between circumferential dikes and eruptive fissures around calderas based on numerical and analog models. *Geophysical Research Letters*, 43(12):6212–6219.

Corbi, F., Rivalta, E., Pinel, V., Maccaferri, F., Bagnardi, M., and Acocella, V. (2015). How caldera collapse shapes the shallow emplacement and transfer of magma in active volcanoes. *Earth and Planetary Science Letters*, 431:287–293.

Cruden, A. and Weinberg, R. (2018). Mechanisms of magma transport and storage in the lower and middle crust—magma segregation, ascent and emplacement. In *Volcanic and Igneous Plumbing Systems*, pages 13–53. Elsevier.

Dahm, T. (2000a). Numerical simulations of the propagation path and the arrest of fluid-filled fractures in the Earth. *Geophysical Journal International*, 141(3):623–638.

Dahm, T. (2000b). On the shape and velocity of fluid-filled fractures in the Earth. *Geophysical Journal International*, 142(1):181–192.

Davis, T. (2021). *Analytische und numerische Untersuchung der dreidimensionalen Ausbreitung von fluidgefüllten Rissen. An analytical and numerical analysis of fluid-filled crack propagation in three dimensions*. PhD thesis, Universität Potsdam.

Davis, T., Bagnardi, M., Lundgren, P., and Rivalta, E. (2021). Extreme curvature of shallow magma pathways controlled by competing stresses: insights from the 2018 sierra negra eruption. *Geophysical Research Letters*, 48(13):e2021GL093038.

Davis, T., Rivalta, E., and Dahm, T. (2020). Critical fluid injection volumes for uncontrolled fracture ascent. *Geophysical Research Letters*, 47(14).

Davis, T., Rivalta, E., Smittarello, D., and Katz, R. F. (2023). Ascent rates of 3-D fractures driven by a finite batch of buoyant fluid. *Journal of Fluid Mechanics*, 954:A12.

Di Vito, M., Lirer, L., Mastrolorenzo, G., and Rolandi, G. (1987). The 1538 Monte Nuovo eruption (Campi flegrei, italy). *Bulletin of Volcanology*, 49(4):608–615.

Di Vito, M. A., Acocella, V., Aiello, G., Barra, D., Battaglia, M., Carandente, A., Del Gaudio, C., De Vita, S., Ricciardi, G. P., Ricco, C., Scandone, R., and Terrasi, F. (2016). Magma transfer at Campi Flegrei caldera (Italy) before the 1538 AD eruption. *Scientific Reports*, 6(1):32245.

Furst, S., Maccaferri, F., and Pinel, V. (2023). Modeling the shape and velocity of magmatic intrusions, a new numerical approach. *Journal of Geophysical Research: Solid Earth*, 128(3):e2022JB025697.

Gudmundsson, A., Pasquarè, F. A., and Tibaldi, A. (2018). Dykes, sills, laccoliths, and inclined sheets in iceland. In Breitkreuz, C. and Rocchi, S., editors, *Physical Geology of Shallow Magmatic Systems*, pages 363–376. Springer International Publishing.

Guidoboni, E. and Ciuccarelli, C. (2011). The campi flegrei caldera: historical revision and new data on seismic crises, bradyseisms, the monte nuovo eruption and ensuing earthquakes (twelfth century 1582 ad). *Bulletin of volcanology*, 73:655–677.

Jaeger, C., Cook, N., and Zimmerman, R. (1969). *Rock mechanics and engineering*. Cambridge University Press, 1 edition.

Lister, J. R. and Kerr, R. C. (1991). Fluid-mechanical models of crack propagation and their application to magma transport in dykes. *Journal of Geophysical Research: Solid Earth*, 96(B6):10049–10077.

Maccaferri, F., Bonafede, M., and Rivalta, E. (2011). A quantitative study of the mechanisms governing dike propagation, dike arrest and sill formation. *Journal of Volcanology and Geothermal Research*, 208(1-2):39–50.

Mantiloni, L., Davis, T., Gaete Rojas, A. B., and Rivalta, E. (2021). Stress inversion in a gelatin box: Testing eruptive vent location forecasts with analog models. *Geophysical Research Letters*, 48(6):e2020GL090407.

Mantiloni, L., Rivalta, E., Anderson, K. R., Davis, T., and Passarelli, L. (2024). Physics-based forecasts of eruptive vent locations at calderas. *Journal of Geophysical Research: Solid Earth*, 129(9):e2023JB028409.

Mantiloni, L., Rivalta, E., and Davis, T. (2023). Mechanical modeling of pre-eruptive magma propagation scenarios at calderas. *Journal of Geophysical Research: Solid Earth*, 128(3):e2022JB025956.

McCarthy, W., Petronis, M. S., Reavy, R. J., and Stevenson, C. T. (2015). Distinguishing diapirs from inflated plutons: an integrated rock magnetic fabric and structural study on the Roundstone Pluton, western Ireland. *Journal of the Geological Society*, 172(5):550–565.

Muller, J. R., Ito, G., and Martel, S. J. (2001). Effects of volcano loading on dike propagation in an elastic half-space. *Journal of Geophysical Research: Solid Earth*, 106(B6):11101–11113.

Nakashima, Y. (1993). Static stability and propagation of a fluid-filled edge crack in rock: implication for fluid transport in magmatism and metamorphism. *Journal of Physics of the Earth*, 41(3):189–202.

Palano, M., Pezzo, G., and Chiarabba, C. (2024). Magma budget, plutonic growth and lateral spreading at Mt. Etna. *Communications Earth & Environment*, 5(1):95.

Parfitt, L. and Wilson, L. (2008). *Fundamentals of physical volcanology*. Wiley-Blackwell.

Pinel, V., Carrara, A., Maccaferri, F., Rivalta, E., and Corbi, F. (2017). A two-step model for dynamical dike propagation in two dimensions: Application to the July 2001 Etna eruption. *Journal of Geophysical Research: Solid Earth*, 122(2):1107–1125.

Pinel, V. and Jaupart, C. (2000). The effect of edifice load on magma ascent beneath a volcano. *Philosophical Transactions of the Royal Society of London. Series A: Mathematical, Physical and Engineering Sciences*, 358(1770):1515–1532.

Rivalta, E. (2021). What pathways for ascending magma? implications for geophysics and petrology. In *VIPS Virtual Seminar Series*.

Rivalta, E. (2024). Dispense dal corso di fisica del vulcanismo. *Laurea magistrale in Fisica del Sistema Terra, Università di Bologna*.

Rivalta, E., Corbi, F., Passarelli, L., Acocella, V., Davis, T., and Di Vito, M. A. (2019). Stress inversions to forecast magma pathways and eruptive vent location. *Science advances*, 5(7):eaau9784.

Rivalta, E., Kavanagh, J., Coombs, M., Hammer, J., Kilgour, G., Passarelli, L., Nikkhoo, M., and Meriaux, C. (2024). Chapter 1: Magma ascent. *The New Encyclopedia of Volcanoes*.

Rivalta, E., Taisne, B., Bunger, A., and Katz, R. (2015). A review of mechanical models of dike propagation: Schools of thought, results and future directions. *Tectonophysics*, 638:1–42.

Rountree, C. L., Kalia, R. K., Lidorikis, E., Nakano, A., Van Brutzel, L., and Vashishta, P. (2002). Atomistic aspects of crack propagation in brittle materials: multimillion atom molecular dynamics simulations. *Annual Review of Materials Research*, 32(1):377–400.

Rubin, A. M. (1993). Dikes vs. diapirs in viscoelastic rock. *Earth and Planetary Science Letters*, 117(3-4):653–670.

Rubin, A. M. (1995). Propagation of magma-filled cracks. *Annual Review of Earth and Planetary Sciences*, 23(1):287–336.

Smith, V., Isaia, R., and Pearce, N. (2011). Tephrostratigraphy and glass compositions of post-15 kyr Campi Flegrei eruptions: implications for eruption history and chronostratigraphic markers. *Quaternary Science Reviews*, 30(25-26):3638–3660.

Smittarello, D. (2019). *Propagation des intrusions basaltiques. Modélisation analogique et suivi temporel par inversion des données de déplacements*. Theses, Université Grenoble Alpes.

Tada, H., Paris, P. C., and Irwin, G. R. (2000). *The stress analysis of cracks handbook, third edition*. ASME Press.

Tait, S. and Taisne, B. (2013). The dynamics of dike propagation. In Fagents, S. A., Gregg, T. K. P., and Lopes, R. M. C., editors, *Modeling Volcanic Processes*, pages 32–54. Cambridge University Press, 1 edition.

Tuffen, H., Smith, R., and Sammonds, P. R. (2008). Evidence for seismogenic fracture of silicic magma. *Nature*, 453(7194):511–514.

Turcotte, D. L. and Schubert, G. (2014). *Geodynamics*. Cambridge University Press, Cambridge, United Kingdom, third edition edition.

Watanabe, T., Masuyama, T., Nagaoka, K., and Tahara, T. (2002). Analog experiments on magma-filled cracks: Competition between external stresses and internal pressure. *Earth, Planets and Space*, 54(12):e1247–e1261.

Weertman, J. (1971). Theory of water-filled crevasses in glaciers applied to vertical magma transport beneath oceanic ridges. *Journal of Geophysical Research*, 76(5):1171–1183.

Weertman, J. (1980). The stopping of a rising, liquid-filled crack in the Earth's crust by a freely slipping horizontal joint. *Journal of Geophysical Research: Solid Earth*, 85(B2):967–976.

Wilding, J. D., Zhu, W., Ross, Z. E., and Jackson, J. M. (2023). The magmatic web beneath Hawai'i. *Science*, 379(6631):462–468.

Wright, T. J., Sigmundsson, F., Pagli, C., Belachew, M., Hamling, I. J., Brandsdóttir, B., Keir, D., Pedersen, R., Ayele, A., Ebinger, C., Einarsson, P., Lewi, E., and Calais, E. (2012). Geophysical constraints on the dynamics of spreading centres from rifting episodes on land. *Nature Geoscience*, 5(4):242–250.